



**AFRL-RX-WP-TP-2011-4385**

**GROWTH STRESS IN SiO<sub>2</sub> DURING OXIDATION OF SiC FIBERS (PREPRINT)**

**Randall S. Hay**

**Ceramics Branch  
Metals, Ceramics & Nondestructive Evaluation Division**

**NOVEMBER 2011**

**Approved for public release; distribution unlimited.**

*See additional restrictions described on inside pages*

**STINFO COPY**

**AIR FORCE RESEARCH LABORATORY  
MATERIALS AND MANUFACTURING DIRECTORATE  
WRIGHT-PATTERSON AIR FORCE BASE, OH 45433-7750  
AIR FORCE MATERIEL COMMAND  
UNITED STATES AIR FORCE**

<b>REPORT DOCUMENTATION PAGE</b>				<i>Form Approved</i> OMB No. 0704-0188	
<p>The public reporting burden for this collection of information is estimated to average 1 hour per response, including the time for reviewing instructions, searching existing data sources, gathering and maintaining the data needed, and completing and reviewing the collection of information. Send comments regarding this burden estimate or any other aspect of this collection of information, including suggestions for reducing this burden, to Department of Defense, Washington Headquarters Services, Directorate for Information Operations and Reports (0704-0188), 1215 Jefferson Davis Highway, Suite 1204, Arlington, VA 22202-4302. Respondents should be aware that notwithstanding any other provision of law, no person shall be subject to any penalty for failing to comply with a collection of information if it does not display a currently valid OMB control number. <b>PLEASE DO NOT RETURN YOUR FORM TO THE ABOVE ADDRESS.</b></p>					
<b>1. REPORT DATE (DD-MM-YY)</b> November 2011		<b>2. REPORT TYPE</b> Technical Paper		<b>3. DATES COVERED (From - To)</b> 1 August 2011 – 1 August 2011	
<b>4. TITLE AND SUBTITLE</b> GROWTH STRESS IN SiO <sub>2</sub> DURING OXIDATION OF SiC FIBERS (PREPRINT)				<b>5a. CONTRACT NUMBER</b> In-house	
				<b>5b. GRANT NUMBER</b>	
				<b>5c. PROGRAM ELEMENT NUMBER</b> 62102F	
<b>6. AUTHOR(S)</b> Randall S. Hay				<b>5d. PROJECT NUMBER</b> 4347	
				<b>5e. TASK NUMBER</b> 50	
				<b>5f. WORK UNIT NUMBER</b> LN102102	
<b>7. PERFORMING ORGANIZATION NAME(S) AND ADDRESS(ES)</b> Ceramics Branch/Metals, Ceramics & Nondestructive Evaluation Division Air Force Research Laboratory, Materials and Manufacturing Directorate Wright-Patterson Air Force Base, OH 45433-7750 Air Force Materiel Command, United States Air Force				<b>8. PERFORMING ORGANIZATION REPORT NUMBER</b> AFRL-RX-WP-TP-2011-4385	
<b>9. SPONSORING/MONITORING AGENCY NAME(S) AND ADDRESS(ES)</b> Air Force Research Laboratory Materials and Manufacturing Directorate Wright-Patterson Air Force Base, OH 45433-7750 Air Force Materiel Command United States Air Force				<b>10. SPONSORING/MONITORING AGENCY ACRONYM(S)</b> AFRL/RXLN	
				<b>11. SPONSORING/MONITORING AGENCY REPORT NUMBER(S)</b> AFRL-RX-WP-TP-2011-4385	
<b>12. DISTRIBUTION/AVAILABILITY STATEMENT</b> Approved for public release; distribution unlimited.					
<b>13. SUPPLEMENTARY NOTES</b> This is a work of the U.S. Government and is not subject to copyright protection in the United States. PA Case Number and clearance date: 88ABW-2011-4233, 3 Aug 2011. This document contains color.					
<b>14. ABSTRACT</b> A method to calculate the three principal growth stresses in SiO <sub>2</sub> scales formed during SiC fiber oxidation has been developed. The method assumes that during oxidation the initial volume expansion at the SiC-SiO <sub>2</sub> interface is three-dimensional and equal in all directions, and that subsequent SiO <sub>2</sub> shear stress relaxation is described by the stress-dependent Eyring viscosity model. Large compressive stresses of ~10 GPa in SiO <sub>2</sub> adjacent to the SiC-SiO <sub>2</sub> interface are relaxed to much lower levels at all temperatures. At 1200° - 1300°C viscous flow of amorphous SiO <sub>2</sub> further relaxes stress to negligible levels. At 700° - 900°C, axial and hoop stress at the GPa level persist. Radial stresses only reach values greater than 100 MPa at 700° - 900°C for scales thicker than ~0.1 fiber radii. Radial expansion of the scale eventually causes hoop stress and later axial stress to become tensile in the outer scale. Differences in stress-states developed for crystallized and uncrystallized scales are considered. Some tentative calculations for crystalline SiO <sub>2</sub> scales are compared with experimental evidence for stress in the crystalline SiO <sub>2</sub> scales of Hi-Nicalon <sup>TM</sup> -S SiC fibers.					
<b>15. SUBJECT TERMS</b> SiC, residual stress, oxidation					
<b>16. SECURITY CLASSIFICATION OF:</b>			<b>17. LIMITATION OF ABSTRACT:</b> SAR	<b>NUMBER OF PAGES</b> 22	<b>19a. NAME OF RESPONSIBLE PERSON (Monitor)</b> Randall S. Hay
<b>a. REPORT</b> Unclassified	<b>b. ABSTRACT</b> Unclassified	<b>c. THIS PAGE</b> Unclassified			
<b>19b. TELEPHONE NUMBER (Include Area Code)</b> N/A					

**Growth Stress in SiO<sub>2</sub> during Oxidation of SiC Fibers**  
**R. S. Hay, Air Force Research Laboratory, WPAFB, OH**

**Abstract**

A method to calculate the three principal growth stresses in SiO<sub>2</sub> scales formed during SiC fiber oxidation has been developed. The method assumes that during oxidation the initial volume expansion at the SiC-SiO<sub>2</sub> interface is three-dimensional and equal in all directions, and that subsequent SiO<sub>2</sub> shear stress relaxation is described by the stress-dependent Eyring viscosity model. Large compressive stresses of ~10 GPa in SiO<sub>2</sub> adjacent to the SiC-SiO<sub>2</sub> interface are relaxed to much lower levels at all temperatures. At 1200° - 1300°C viscous flow of amorphous SiO<sub>2</sub> further relaxes stress to negligible levels. At 700° - 900°C, axial and hoop stress at the GPa level persist. Radial stresses only reach values greater than 100 MPa at 700° - 900°C for scales thicker than ~0.1 fiber radii. Radial expansion of the scale eventually causes hoop stress and later axial stress to become tensile in the outer scale. Differences in stress-states developed for crystallized and uncrystallized scales are considered. Some tentative calculations for crystalline SiO<sub>2</sub> scales are compared with experimental evidence for stress in the crystalline SiO<sub>2</sub> scales of Hi-Nicalon<sup>TM</sup>-S SiC fibers. Assumptions and limitations of the method are discussed, along with implications for fiber strength and oxidation kinetics.

**I. Introduction**

Passive oxidation of SiC to SiO<sub>2</sub> is in most cases controlled by interstitial diffusion of O<sub>2</sub> molecules through the amorphous or crystalline silica scale.<sup>1-2</sup> There is a volume expansion of ~2.2x during SiC oxidation to SiO<sub>2</sub>. Constraint of this expansion at the SiC-SiO<sub>2</sub> interface generates very large stresses. Microstructural evidence for these stresses exists for crystalline scales. Cracks formed in crystalline scales during SiC fiber oxidation were attributed to tensile hoop growth stress in the outer scale.<sup>3-5</sup> These cracks function as short-circuit diffusion pathways for oxidation and render the scale non-passivating.<sup>5-6</sup> Tensile stress in the scale may also contribute to lower strengths during oxidation at high temperature.<sup>7</sup> Very high dislocation densities in crystalline SiO<sub>2</sub> near the SiC-SiO<sub>2</sub> interface scales suggests that very high shear stresses exist during scale growth near that interface.<sup>5</sup>

Oxidation of silicon to SiO<sub>2</sub> has a volume expansion similar to that for SiC oxidation. Large effort has been devoted to modeling growth stress during silicon oxidation at 700° - 1200°C.<sup>8</sup> These studies are motivated by the use of SiO<sub>2</sub> as a dielectric and a device isolation material in integrated circuits.<sup>9-10</sup> Numerical models using finite element or finite difference methods that are adaptable to a variety of silicon substrate geometries in integrated circuits have been developed to model oxidation growth stress.<sup>8-9, 11-19</sup> Analytical models for flat-plate and cylindrical silicon substrates have also been developed that predict differences in the growth stresses for the two geometries. Radial and axial compressive growth stress and tensile hoop growth stress are predicted for oxidation of silicon fibers.<sup>20-22</sup> For the flat plate geometry, only in-plane compressive growth stress is present.

The role of growth stress on oxidation mechanisms in silicon has been extensively analyzed and discussed.<sup>23</sup> Compressive growth stress reduces O<sub>2</sub> diffusivity in SiO<sub>2</sub>,<sup>8, 12, 20, 24-25</sup> reducing Si oxidation rates.<sup>26-28</sup> Externally applied compressive stress has also been shown to decrease the rate of silicon oxidation.<sup>29</sup> Externally applied tensile stress increases those oxidation rates,<sup>29-31</sup> and recently the same has been demonstrated for SiC fibers.<sup>32</sup> However, growth stress modeling and analysis for SiC oxidation is lacking. Extensive characterization and analysis of carbon and SiOC layer formation at the SiC-SiO<sub>2</sub> interface during SiC oxidation has not considered the effects of growth stress.<sup>2</sup> Growth stress also contributes to the residual stress in SiO<sub>2</sub> scales on SiC fibers, which in turn may affect the crystallization rates of the scales and the strengths of oxidized fibers.<sup>5</sup>

Existing growth stress models for cylindrical silicon substrates assume that the volume expansion accompanying oxidation is either dilational (equal expansion in all directions),<sup>7</sup> uniaxial (all expansion in the radial direction),<sup>7, 33-34</sup> or nearly uniaxial but with a small intrinsic axial and hoop strain in the SiO<sub>2</sub> oxidation product.<sup>20, 25</sup> Most models assume stress is two-dimensional and ignore the axial stress ( $\sigma_z$ ).<sup>21, 25, 33-34</sup> However, silicon wafer bending during oxidation can only be explained by three-dimensional expansion during oxidation.<sup>8, 10</sup> Early cylinder oxidation models assumed Newtonian viscous flow.<sup>7, 21, 33</sup> Most later models recognize that flow at high stress is non-Newtonian and use the Eyring model for stress-dependent viscosity.<sup>20, 25, 34</sup> Uniaxial expansion models with Newtonian flow predict high tensile hoop stress ( $\sigma_\theta$ ) at the SiC-SiO<sub>2</sub> interface that decreases towards the SiO<sub>2</sub> surface.<sup>7, 21, 33</sup> Models with stress-dependent viscosity predict compressive  $\sigma_\theta$  at the SiC-SiO<sub>2</sub> interface that rapidly

changes to tension towards the SiO<sub>2</sub> surface.<sup>20, 34</sup> One model with stress-dependent viscosity considers only shear stress and does not attempt to resolve it into principal stresses.<sup>25</sup> No models calculate both  $\sigma_z$  and  $\sigma_\theta$  for cylindrical substrates, or consider how the change in  $\sigma_\theta$  from compressive to tensile affects shear stress, and how the relaxation of shear stress then separately affects  $\sigma_\theta$  and  $\sigma_z$ . For structural SiC fibers this is an important omission because the  $\sigma_z$  component of residual stress that may affect fiber strength.

A method for computation of all three principal growth stresses throughout the thickness of an SiO<sub>2</sub> scale during oxidation of SiC fibers is presented. The method can be equally well applied to silicon fibers or cylinders. The model assumes oxidation volume expansion is three-dimensional (dilatational) and that the stresses resulting from constraint of that expansion are relaxed with an Eyring stress-dependent SiO<sub>2</sub> viscosity.<sup>35</sup> Growth stress calculations for oxidation of SiC fibers are done from 700° to 1300°C for amorphous scale thicknesses up to 3 μm. Some calculations are also done for crystalline scales using the very limited data available for cristobalite viscosity.<sup>36-38</sup> These calculations are compared with microstructural evidence for stress in crystalline scales on Hi-Nicalon™-S SiC fibers that has been previously published.<sup>5</sup> Possible effects of self stress on O<sub>2</sub> diffusion are discussed. The change in oxidation growth stress with fiber radii from 3 μm to  $\rightarrow \infty$  (flat plate) are examined. Assumptions and limitations of the model are discussed.

## II. Method

### A. General

A schematic illustrating the volume expansion and the stresses associated with oxidation, as well as the discretization of SiC oxidation into annular SiO<sub>2</sub> layers is shown in **figure 1**. There are two sources of stress. The first is the 2.2× volume expansion from oxidation of SiC to SiO<sub>2</sub>. This expansion is shown in stress-free and constrained states in **figure 1**. Constraint of that expansion by the underlying SiC and overlying SiO<sub>2</sub> causes extremely large axial ( $\sigma_z$ ) and hoop ( $\sigma_\theta$ ) stress, and much smaller radial ( $\sigma_r$ ) stress because  $\sigma_r = 0$  at the scale surface and small scale thicknesses relative to fiber radii are usually of interest.  $\sigma_r$  increases or decreases through the scale thickness, depending on the sign and magnitude of  $\sigma_z$  and  $\sigma_\theta$ . The stresses involved in constraint of the initial volume expansion are far larger than those for which linear elasticity theory is valid.<sup>8</sup> However, as pointed out previously,<sup>25</sup> even at low temperatures  $\sigma_z$  and  $\sigma_\theta$  relax very rapidly from high levels by radial expansion to values appropriate for linear elasticity if the Eyring model for the dependence of viscosity on shear stress is used. The second source of stress is the circumferential expansion of old scale as it is radially displaced by the formation of new scale (**Fig. 1**). This creates tensile  $\sigma_\theta$  in the older scale and eventually tensile  $\sigma_z$  by the Poisson effect.

A flowchart with the major calculation steps is shown in **figure 2**. A detailed description of the calculation methods in each step follows.

### B. SiC Fiber Oxidation Kinetics

Fiber oxidation kinetics do not deviate significantly from those for flat plate geometry until the oxidation products for 12 μm diameter fibers are several microns thick,<sup>5, 39</sup> so SiO<sub>2</sub> thickness [**w(t)**] (**Fig. 1**) is assumed to obey Deal-Grove kinetics for flat plate geometry:<sup>5, 40</sup>

$$w(t) = \frac{1}{2}A \sqrt{1 + \frac{4B(t + t_i)}{A^2}} - 1 \quad [1a]$$

$$t_i = \frac{x_i^2 + Ax_i}{B} \quad [1b]$$

where  $t_i$  is a time shift that corrects for the presence of an initial oxide layer  $x_i$ ,  $B$  is the parabolic rate constant and  $B/A$  is the linear rate constant. All growth stress modeling for amorphous SiO<sub>2</sub> assumes that  $x_i=0$ , but for crystalline scales it is useful to consider the thickness at which the scale crystallizes as a stress-free state with thickness  $x_i$ .  $B$  and  $A$  obey the usual Arrhenius relationships:

$$A = A_0 e^{\frac{-Q_A}{RT}} \quad [2]$$

$$B = B_0 e^{\frac{-Q_B}{RT}}$$

[3]

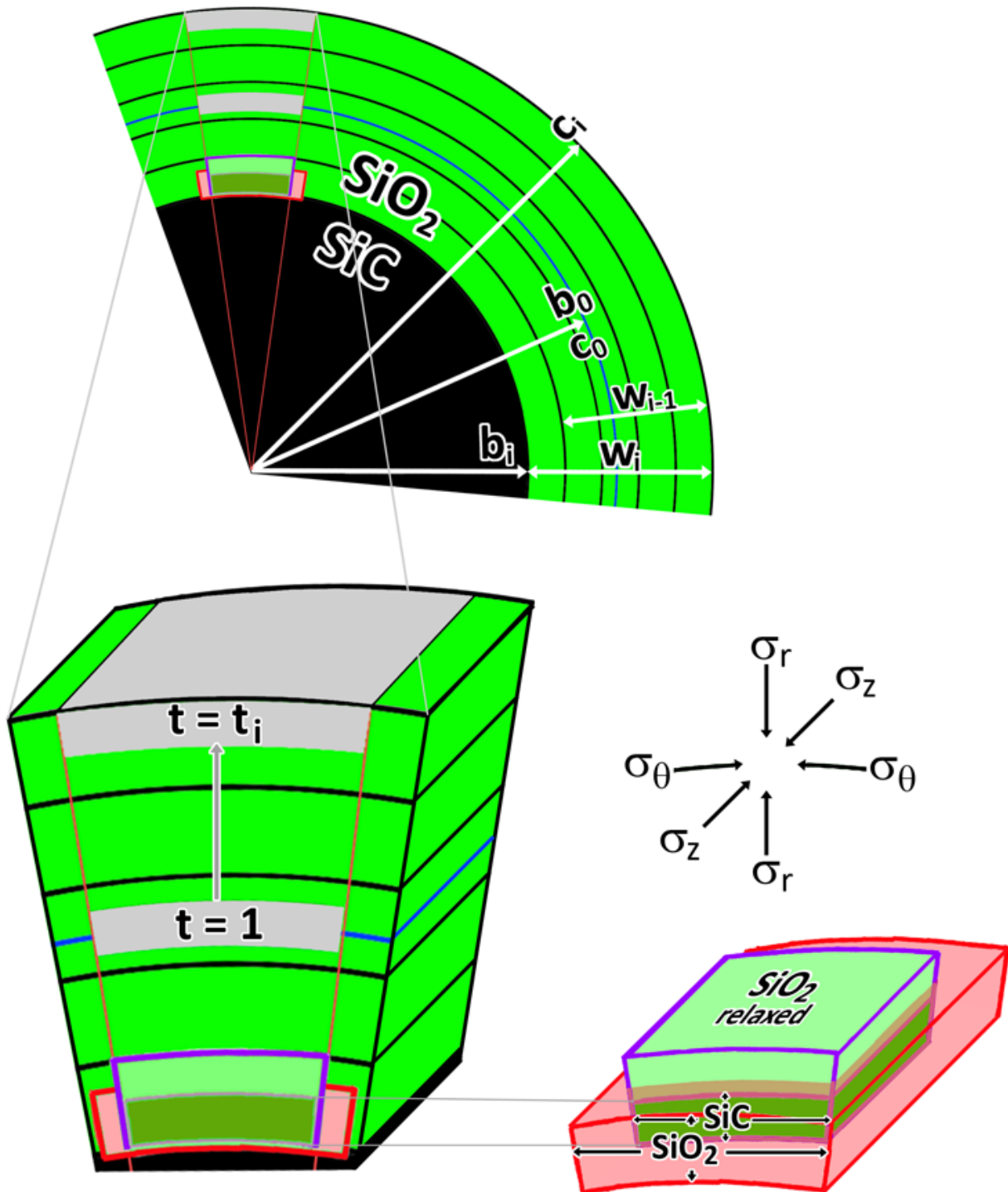
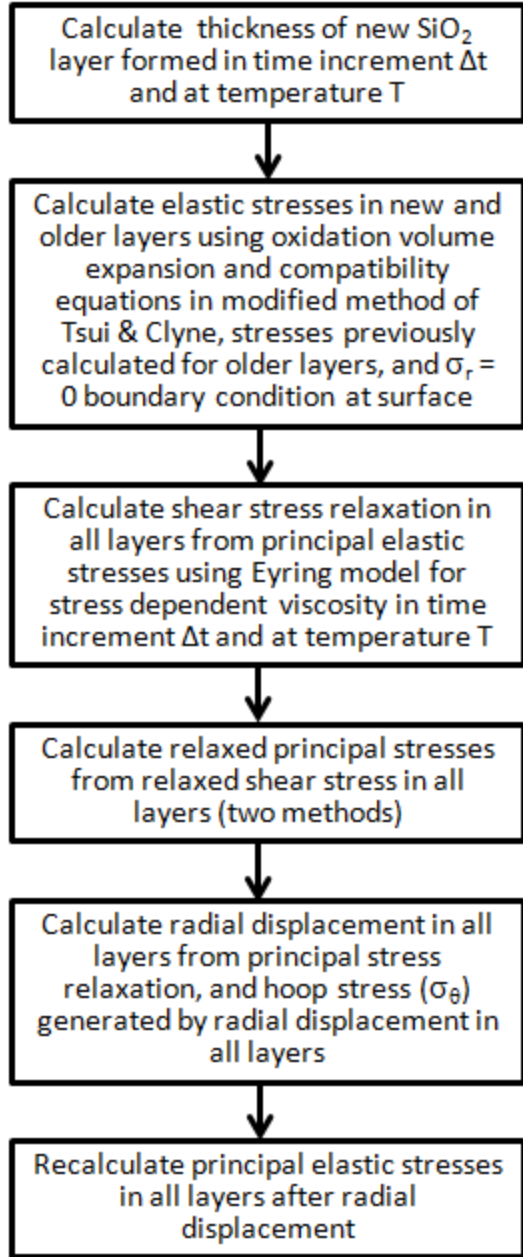


**Fig. 1** Schematic diagrams of oxidation of SiC to SiO<sub>2</sub>. Discretization of annular layers is illustrated and notated. Volume expansions and stresses associated with oxidation are indicated. The circumferential expansion of an old scale layer as it is pushed outward is also shown. The original SiC surface is shown as a blue line, roughly midway through the scale thickness. Original SiC is dark green, the elastically constrained SiO<sub>2</sub> oxidation product is light red, and the relaxed SiO<sub>2</sub> is light green with a purple boundary.



growth stresses during SiC fiber oxidation.

The axial, radial, and hoop stresses in the two annular SiO<sub>2</sub> layers are  $\sigma_z^{\text{SiO}_2}(i-1)$ ,  $\sigma_r^{\text{SiO}_2}(i-1)$ ,  $\sigma_\theta^{\text{SiO}_2}(i-1)$ , respectively. The increment in SiO<sub>2</sub> thickness formed from time  $t=i-1$  to  $t=i$  is therefore  $w(i)-w(i-1)$ . The effect of adding the  $i^{\text{th}}$  SiO<sub>2</sub> layer on the principal stresses in the three separate volumes can be found from three equations for  $f$ ,  $p_j$ , and  $p_{is}$ , using a modification of the method of Tsui and Clyne that uses strain compatibility equations:<sup>41</sup>

$$E_{\text{SiO}_2} \Delta \varepsilon = \sigma_z^{\text{SiO}_2}(i-1) - \sigma_z^{\text{SiO}_2}(i) + \nu_{\text{SiO}_2} \left( \sigma_\theta^{\text{SiO}_2}(i) - \sigma_\theta^{\text{SiO}_2}(i-1) + \sigma_r^{\text{SiO}_2}(i) - \sigma_r^{\text{SiO}_2}(i-1) \right) \quad [7]$$

$$E_{\text{SiO}_2} \Delta \varepsilon = \sigma_\theta^{\text{SiO}_2}(i-1) - \sigma_\theta^{\text{SiO}_2}(i) + \nu_{\text{SiO}_2} \left( \sigma_z^{\text{SiO}_2}(i) - \sigma_z^{\text{SiO}_2}(i-1) + \sigma_r^{\text{SiO}_2}(i) - \sigma_r^{\text{SiO}_2}(i-1) \right) \quad [8]$$

where  $T$  is absolute temperature,  $R$  is the gas constant,  $Q_A$  and  $Q_B$  are activation energies and  $A_0$  and  $B_0$  are pre-exponential factors. Recent work finds that  $A_0 = 4.7 \times 10^{-4}$  m,  $Q_A = 110$  kJ/mol,  $B_0 = 1.2 \times 10^{-8}$  m<sup>2</sup>/s,  $Q_B = 248$  kJ/mol for Hi-Nicalon<sup>TM</sup>-S SiC fiber oxidation.<sup>5</sup> The SiO<sub>2</sub> oxidation product has  $2.2 \times$  the volume of the SiC consumed. The SiC radius  $[b(t)]$  after oxidation for time  $t$  is (Fig. 1):

$$b(t) = \sqrt{w^2(\Omega^2 - \Omega) + b_0^2} - \Omega w \quad [4]$$

where  $b_0$  is the original fiber radius (6.1 μm for Hi-Nicalon<sup>TM</sup>-S)<sup>5</sup> and  $\Omega$  is the ratio of SiC molar volume ( $\Omega_{\text{SiC}}$ ) to SiO<sub>2</sub> molar volume ( $\Omega_{\text{SiO}_2}$ ), sometimes referred to as the Pilling-Bedworth ratio:

$$\Omega = \frac{\Omega_{\text{SiC}}}{\Omega_{\text{SiO}_2}} = \frac{12.46 \text{ cm}^3}{27.34 \text{ cm}^3} = 0.456 \quad [5]$$

The outer radius of the SiO<sub>2</sub> scale  $[c(t)]$  is (Fig. 1):

$$c(t) = b(t) + w(t) \quad [6]$$

### C. Elastic Growth Stress

The elastic stresses and strains can be determined from a modification of a method used for progressively deposited coatings on cylinders.<sup>41</sup> This method was developed for sequentially deposited coatings, where the last coating is at the surface. During fiber oxidation the “deposition” sequence is reversed; the last oxide increment forms at the SiC-SiO<sub>2</sub> interface. The SiO<sub>2</sub> scale is therefore discretized into annular increments, or layers, formed in equal units of time, with the oldest layer at the surface.

The unrelaxed elastic growth stresses are calculated by dividing the SiC-SiO<sub>2</sub> system into three separate volumes – the unoxidized SiC fiber, the annular SiO<sub>2</sub> added from time  $t(i-1)$  to  $t(i)$  at the SiC-SiO<sub>2</sub> interface, and the outer (older) SiO<sub>2</sub> ring that was added from time  $t(0)$  to  $t(i-1)$  (Fig. 1). The axial, radial, and hoop stresses in the SiC fiber at time  $t(i)$  are designated  $\sigma_z^{\text{SiC}}(i)$ ,  $\sigma_r^{\text{SiC}}(i)$ , and  $\sigma_\theta^{\text{SiC}}(i)$  respectively.

The axial, radial, and hoop stresses in the two annular SiO<sub>2</sub> layers are  $\sigma_z^{\text{SiO}_2}(i)$ ,  $\sigma_r^{\text{SiO}_2}(i)$ ,  $\sigma_\theta^{\text{SiO}_2}(i)$  and  $\sigma_z^{\text{SiO}_2}(i-1)$ ,  $\sigma_r^{\text{SiO}_2}(i-1)$ ,  $\sigma_\theta^{\text{SiO}_2}(i-1)$ , respectively. The increment in SiO<sub>2</sub> thickness formed from time  $t=i-1$  to  $t=i$  is therefore  $w(i)-w(i-1)$ . The effect of adding the  $i^{\text{th}}$  SiO<sub>2</sub> layer on the principal stresses in the three separate volumes can be found from three equations for  $f$ ,  $p_j$ , and  $p_{is}$ , using a modification of the method of Tsui and Clyne that uses strain compatibility equations:<sup>41</sup>

$$\frac{1}{E_{\text{SiO}_2}} \left[ \sigma_{\theta}^{\text{SiO}_2}(i) - \nu_{\text{SiO}_2} \left( \sigma_z^{\text{SiO}_2}(i) + \sigma_r^{\text{SiO}_2}(i) \right) \right] = \frac{1}{E_{\text{SiC}}} \left[ \sigma_{\theta}^{\text{SiC}}(i) - \nu_{\text{SiC}} \left( \sigma_z^{\text{SiC}}(i) + \sigma_r^{\text{SiC}}(i) \right) \right] \quad [9]$$

where:

$$\Delta \varepsilon = \sqrt[3]{\frac{\Omega_{\text{SiO}_2}}{\Omega_{\text{SiC}}}} - 1 \quad [10]$$

$$\sigma_z^{\text{SiC}}(i) = \frac{-E_{\text{SiC}} f}{\pi \left( E_{\text{SiC}} b^2(i) + E_{\text{SiO}_2} \left( (b(i) + w(i) - w(i-1))^2 - b^2(i) \right) \right)} + \sigma_z^{\text{SiC}}(i-1) \quad [11]$$

$$\sigma_r^{\text{SiC}}(i) = \sigma_r^{\text{SiC}}(i-1) - p_{\text{is}} \quad [12]$$

$$\sigma_{\theta}^{\text{SiC}}(i) = \sigma_{\theta}^{\text{SiC}}(i-1) - p_{\text{is}} \quad [13]$$

$$\sigma_z^{\text{SiO}_2}(i) = \frac{-E_{\text{SiO}_2} f}{\pi \left( E_{\text{SiC}} b(i)^2 + E_{\text{SiO}_2} \left( (b(i) + w(i))^2 - b(i)^2 \right) \right)} \quad [14]$$

$$\sigma_r^{\text{SiO}_2}(i) = -p_i \quad [15]$$

$$\sigma_{\theta}^{\text{SiO}_2}(i) = \frac{p_i (b(i) + w(i))}{w(i) - w(i-1)} \quad [16]$$

$$\sigma_z^{\text{SiO}_2}(i-1) = \frac{f}{\pi \left[ (b(i-1) + w(i-1) - w(i))^2 - b^2(i-1) \right]} \quad [17]$$

$$\sigma_r^{\text{SiO}_2}(i-1) = 0 \quad [18]$$

$$\sigma_{\theta}^{\text{SiO}_2}(i-1) = \frac{2p_{\text{is}} b(i-1)^2 - p_i \left( (b(i-1) + w(i-1))^2 + b(i-1)^2 \right)}{(b(i-1) + w(i-1))^2 - b(i-1)^2} \quad [19]$$

where  $f$  is the axial force,  $p_{\text{is}}$  is the pressure across the SiO<sub>2</sub>-SiC interface,  $p_i$  is the pressure across the interface between the  $i^{\text{th}}$  and the  $(i-1)^{\text{th}}$  SiO<sub>2</sub> layers,  $E_{\text{SiC}}$  and  $E_{\text{SiO}_2}$  and Young's modulus of the SiC fiber and the SiO<sub>2</sub> scale, respectively, and  $\nu_{\text{SiC}}$  and  $\nu_{\text{SiO}_2}$  are Poisson's ratio for the SiC fiber and the SiO<sub>2</sub> scale.

Stresses in older layers ( $j = i-2$  to  $j = 0$ ) are updated with the  $i-1$  stress values in [17 - 19]:

$$\sigma_z^{\text{SiO}_2}(j) = \sigma_z^{\text{SiO}_2}(j) + \sigma_z^{\text{SiO}_2}(i-1) \quad [20]$$

$$\sigma_r^{\text{SiO}_2}(j) = \sigma_r^{\text{SiO}_2}(j) + \sigma_r^{\text{SiO}_2}(i-1) \quad [21]$$

$$\sigma_{\theta}^{\text{SiO}_2}(j) = \sigma_{\theta}^{\text{SiO}_2}(j) + \sigma_{\theta}^{\text{SiO}_2}(i-1) \quad [22]$$

#### D. Relaxation of Shear Stress

The relaxation of the elastic stresses for all annular elements ( $j=1$  to  $i$ ) in time increment  $\Delta t = t(i) - t(i-1)$  are calculated next. Stress relaxation in the SiC substrate is assumed to be negligible. Deviation

from Newtonian viscosity, referred to as glass plasticity, results in lower effective viscosity at high shear stress. The Eyring model for shear stress ( $\tau$ ) dependence of glass viscosity ( $\eta$ ) is frequently used for viscosity:<sup>8-9, 11-12, 14, 16, 18-20, 22, 25, 35, 42</sup>

$$\eta = \eta_0 \frac{\tau V_c / 2kT}{\text{Sinh}(\tau V_c / 2kT)} = \eta_0 \frac{\tau / \tau_c}{\text{Sinh}(\tau / \tau_c)} \quad [23]$$

where the activation volume for plasticity in  $\text{SiO}_2$ ,  $V_c$ , decreases with temperature, and has been inferred to have values ranging between  $1.2 \times 10^{-28} \text{ m}^3$  to  $3 \times 10^{-28} \text{ m}^3$ .<sup>12, 20, 25</sup> The parameter  $k$  is Boltzmann's constant,  $\tau_c$  is the critical shear stress above which plasticity is significant (typically  $\sim 150$  MPa), and  $\eta_0$  is the stress-free viscosity described by:<sup>43-44</sup>

$$\eta_0 = C_0 e^{\frac{Q}{RT}}, \quad C_0 = 3.8 \times 10^{-13} \text{ \& } Q = 712,000 \text{ kJ/mol} \quad [24]$$

from 1000°C to 1400°C. Unfortunately this relationship lacks experimental validation below 1000°C.<sup>43-44</sup> For silica formed from SiC oxidation, carbon in the  $\text{SiO}_2$  scale may cause viscosities to be higher than those in [24].<sup>45</sup> The plasticity activation volume  $V_c$  corresponds to a critical shear stress  $\tau_c$  of about 100 MPa, which is roughly consistent with experiment at 500 to 1400°C.<sup>42, 46</sup> Shear stress relaxation with time obeys a Maxwell viscoelastic model:<sup>12, 25, 47</sup>

$$\frac{d\tau(t)}{dt} = -G \tau(t) / \eta(\tau), \quad \tau[t(i-1)] = \tau_0 t(i-1) \quad [25]$$

where  $G$  is the  $\text{SiO}_2$  shear modulus and the shear stress at the initial time  $t(i-1)$  is  $\tau_0$ . The shear modulus ( $G$ ) of amorphous silica is 34 GPa, with only weak temperature dependence.<sup>48</sup> The relaxation of shear stress with time ( $\tau(t)$ ) can be determined by substitution of [23-24] in [25] and solving the resulting differential equation [25] for  $\tau[t]$ :

$$\tau[t] = \frac{4kT}{V_c} \text{Coth}^{-1} \left[ \frac{\frac{Gt}{e^{\eta_0}}}{\sqrt{\text{Tanh} \left[ \frac{V_c \tau_0}{4kT} \right]^2}} \right] = 2\tau_c \text{Coth}^{-1} \left[ \frac{\frac{Gt}{e^{\eta_0}}}{\sqrt{\text{Tanh} \left[ \frac{\tau_0}{2\tau_c} \right]^2}} \right] \quad [26]$$

The initial shear stress  $\tau_0$  is determined from the principal stresses for all the separate annular elements ( $j=1$  to  $i$ ) by the usual method:

$$\tau_0 = \frac{1}{2} (\sigma_1(j) - \sigma_3(j)) \quad [27]$$

where  $\sigma_1(j)$ ,  $\sigma_2(j)$ , and  $\sigma_3(j)$  are the maximum, intermediate, and minimum principal stresses of the  $j^{\text{th}}$  annular element at time  $t(j)$  determined from values for  $\sigma_z^{\text{SiO}_2}(j)$ ,  $\sigma_r^{\text{SiO}_2}(j)$ , and  $\sigma_\theta^{\text{SiO}_2}(j)$ .

#### E. Determination of Relaxed Principal Stresses from Relaxed Shear Stress

Calculation of the relaxation of the principal stresses from relaxation of the shear stress  $\tau_0$  to  $\tau(t)$  in equation [26] is complicated by the presence of both tensile and compressive principal stresses. It is therefore also useful to designate principal stresses by their rank in absolute value as  $^1\sigma(j)$ ,  $^2\sigma(j)$ , and  $^3\sigma(j)$ , and to define:

$$\delta[\sigma(j)] = \begin{cases} 1 & \sigma(j) > 0 \\ -1 & \sigma(j) < 0 \end{cases} \quad [28]$$

A boundary condition is  $\sigma_r^{\text{SiO}_2}(1) = 0$ , but  $\sigma_r^{\text{SiO}_2}(j>1)$  will have a small negative value (compression) if  $\sigma_z^{\text{SiO}_2}(j>1)$  and  $\sigma_\theta^{\text{SiO}_2}(j>1)$  are positive (tension), or a positive value if the other principal stresses are negative. Since the scale is free to expand in the radial direction, volume is not conserved,

and decomposition of the stress tensor into hydrostatic and deviatoric components, as used for some growth stress calculations,<sup>13-14</sup> is not useful because the hydrostatic pressure can change with relaxation. In almost all cases  $\sigma_r^{SiO_2}(j)$  will be  ${}^3\sigma(j)$ , but there are some exceptions when  $\sigma_z^{SiO_2}(j)$  or  $\sigma_\theta^{SiO_2}(j)$  are changing from compressive (negative) to tensile (positive) and are therefore  ${}^3\sigma(j)$  for a relatively short period of time. The different relationships between  $\sigma_{1,2,3}(j)$  and  ${}^{1,2,3}\sigma(j)$  are shown in **figure 3**, and require differences in the way new principal stresses  $[\sigma(j)']$  are calculated after shear stress relaxation. Two methods are employed. The first assumes that only  ${}^1\sigma(j)$  will relax, until it reaches the value for  ${}^2\sigma(j)$ , at which point both relax. This method is best suited for high  $\tau$  where  $\eta$  [23] is not Newtonian, and is later referenced as the “High  $\tau$  Method”.  $\sigma_r^{SiO_2}(j)$  is a boundary condition unless  $|\sigma_r^{SiO_2}(j)| \leq |\sigma_z^{SiO_2}(j)|$  &  $|\sigma_\theta^{SiO_2}(j)|$ , where the boundary condition becomes 0 for all stresses. For principal stresses of type ( ${}^1\sigma_1$ ,  ${}^2\sigma_2$ ,  ${}^3\sigma_3$ ) or ( ${}^3\sigma_1$ ,  ${}^2\sigma_2$ ,  ${}^1\sigma_3$ ):

$$\text{If } 2\tau(j) > |{}^2\sigma(j) - {}^3\sigma(j)| : \quad \begin{aligned} {}^1\sigma(j)' &= {}^3\sigma(j) + 2\delta[{}^1\sigma(j)]\tau \\ {}^2\sigma(j)' &= {}^2\sigma(j) \\ {}^3\sigma(j)' &= {}^3\sigma(j) \end{aligned} \quad [29]$$

$$\text{If } 2\tau(j) < |{}^2\sigma(j) - {}^3\sigma(j)| \text{ \& } \delta[{}^2\sigma(j)] = \delta[{}^3\sigma(j)] : \quad \begin{aligned} {}^1\sigma(j)' &= {}^3\sigma(j) + 2\delta[{}^1\sigma(j)]\tau \\ {}^2\sigma(j)' &= {}^3\sigma(j) + 2\delta[{}^1\sigma(j)]\tau \\ {}^3\sigma(j)' &= {}^3\sigma(j) \end{aligned} \quad [30]$$

$$\text{If } 2\tau(j) < |{}^2\sigma(j) - {}^3\sigma(j)| \text{ \& } \delta[{}^2\sigma(j)] \neq \delta[{}^3\sigma(j)] \text{ \& } \tau(j) > |{}^3\sigma| : \quad \begin{aligned} {}^1\sigma(j)' &= {}^3\sigma(j) + 2\delta[{}^1\sigma(j)]\tau \\ {}^2\sigma(j)' &= {}^3\sigma(j) + 2\delta[{}^1\sigma(j)]\tau \\ {}^3\sigma(j)' &= {}^3\sigma(j) \end{aligned} \quad [31]$$

$$\text{If } 2\tau(j) < |{}^2\sigma(j) - {}^3\sigma(j)| \text{ \& } \delta[{}^2\sigma(j)] \neq \delta[{}^3\sigma(j)] \text{ \& } \tau(j) < |{}^3\sigma| : \quad \begin{aligned} {}^1\sigma(j)' &= \delta[{}^1\sigma(j)]\tau \\ {}^2\sigma(j)' &= \delta[{}^2\sigma(j)]\tau \\ {}^3\sigma(j)' &= \delta[{}^3\sigma(j)]\tau \end{aligned} \quad [32]$$

For all other principal stresses:

$$\text{If } \tau(j) > |{}^2\sigma(j)| : \quad \begin{aligned} {}^1\sigma(j)' &= {}^2\sigma(j) + 2\delta[{}^1\sigma(j)]\tau \\ {}^2\sigma(j)' &= {}^2\sigma(j) \\ {}^3\sigma(j)' &= {}^3\sigma(j) \end{aligned} \quad [33]$$

$$\text{If } |{}^2\sigma(j)| > \tau(j) > |{}^3\sigma(j)| : \quad \begin{aligned} {}^1\sigma(j)' &= \delta[{}^1\sigma(j)]\tau \\ {}^2\sigma(j)' &= \delta[{}^2\sigma(j)]\tau \\ {}^3\sigma(j)' &= {}^3\sigma(j) \end{aligned} \quad [34]$$

$$\text{If } \tau(j) < |{}^3\sigma(j)| : \quad \begin{aligned} {}^1\sigma(j)' &= \delta[{}^1\sigma(j)]\tau \\ {}^2\sigma(j)' &= \delta[{}^2\sigma(j)]\tau \\ {}^3\sigma(j)' &= \delta[{}^3\sigma(j)]\tau \end{aligned} \quad [35]$$

This method is consistent with radial expansion at a free surface with minimization of strain energy through minimization of  ${}^1\sigma(j)^2 + {}^2\sigma(j)^2 + {}^3\sigma(j)^2$ . The relaxed values of  ${}^1\sigma(j)'$ ,  ${}^2\sigma(j)'$ , and  ${}^3\sigma(j)'$  are reassigned to  $\sigma_z^{SiO_2}(j)$ ,  $\sigma_r^{SiO_2}(j)$ , and  $\sigma_\theta^{SiO_2}(j)$ .

The second method assumes that viscosity is Newtonian and that the rate of  $\sigma_\theta(j)$  and  $\sigma_z(j)$  relaxation is proportional to their difference with  $\tau(t)/\tau_0$  and  $\sigma_r(j)$ , which is a boundary condition and does not change, being zero at the SiO<sub>2</sub> surface and near zero elsewhere. This method is best suited for high temperatures and low shear stresses where  $\eta$  is Newtonian, and is later referenced as the “Low  $\tau$  Method”.  $\sigma_\theta(j)'$  and  $\sigma_z(j)'$  can be determined by solution of:

$$\begin{bmatrix} \sigma_\theta(j)' & 0 & 0 \\ 0 & \sigma_z(j)' & 0 \\ 0 & 0 & \sigma_r(j) \end{bmatrix} = \frac{\tau(t)}{\tau_0} \begin{bmatrix} \sigma_\theta(j) - \sigma_r(j) & 0 & 0 \\ 0 & \sigma_z(j) - \sigma_r(j) & 0 \\ 0 & 0 & \sigma_r(j) \end{bmatrix} + \begin{bmatrix} \sigma_r(j) & 0 & 0 \\ 0 & \sigma_r(j) & 0 \\ 0 & 0 & \sigma_r(j) \end{bmatrix} \quad [36]$$

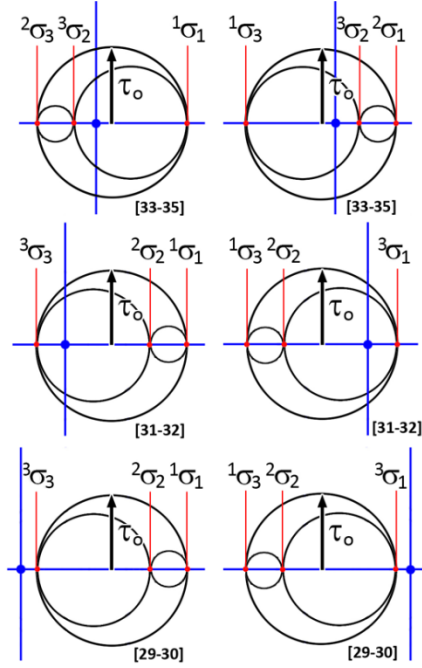


**Fig. 3** The relationships between the magnitudes ( $\sigma_i$ ) and absolute value magnitudes ( $\sigma$ ) of the principal growth stresses that are used to calculate principal stress relaxation from shear stress relaxation in [29] – [35].

At very low principal stresses, where  $|\sigma_r^{\text{SiO}_2}(j)| \geq |\sigma_z^{\text{SiO}_2}(j)|$  &  $|\sigma_\theta^{\text{SiO}_2}(j)|$  and they are opposite in sign,  $|\sigma_z^{\text{SiO}_2}(j)|$  and  $|\sigma_\theta^{\text{SiO}_2}(j)|$  increase, and this method is therefore inconsistent with minimization of strain energy. However, this condition can only occur very briefly when  $\sigma_z^{\text{SiO}_2}(j)$  and  $\sigma_\theta^{\text{SiO}_2}(j)$  change from compressive to tensile from radial displacement of the scale, described next.

#### F. Radial Displacement and Hoop Stress Generation in Scale

Relaxation expands the  $\text{SiO}_2$  scale radially. The individual radial displacement of the  $j$ th layer ( $\mathbf{u}_r(j)$ ) is:

$$u_r(j) = \frac{\Omega_{\text{SiO}_2}}{\Omega_{\text{SiC}} \left( 1 + \varepsilon_z^{\text{SiO}_2}(j) + \varepsilon_\theta^{\text{SiO}_2}(j) + \varepsilon_z^{\text{SiO}_2}(j)\varepsilon_\theta^{\text{SiO}_2}(j) \right)} - 1 \quad [37]$$

where

$$\varepsilon_z^{\text{SiO}_2}(j) = \frac{1}{E_{\text{SiO}_2}} \left[ \sigma_z^{\text{SiO}_2}(j) - \nu_{\text{SiO}_2} \left( \sigma_\theta^{\text{SiO}_2}(j) + \sigma_r^{\text{SiO}_2}(j) \right) \right] \quad [38]$$

$$\varepsilon_\theta^{\text{SiO}_2}(j) = \frac{1}{E_{\text{SiO}_2}} \left[ \sigma_\theta^{\text{SiO}_2}(j) - \nu_{\text{SiO}_2} \left( \sigma_z^{\text{SiO}_2}(j) + \sigma_r^{\text{SiO}_2}(j) \right) \right] \quad [39]$$

The radial displacement of the  $j^{\text{th}}$  outer layer is equal to the sum of the radial displacements of all the younger layers ( $i-j-1$ ) beneath it. This adds hoop strain ( $\varepsilon_\theta^{\text{SiO}_2}$ ) to outer, older layers as they are displaced radially outward and forced to a larger circumference (Fig. 1). The new hoop strain in each layer can be calculated from the sum:

$$\varepsilon_\theta^{\text{SiO}_2}(j) = \varepsilon_\theta^{\text{SiO}_2}(j) + \sum_j^i u_r(j) \frac{b(j-1) - b(j)}{b(j)} \quad [40]$$

where

$$w(i) - w(i-1) = \sum_{i-1}^i u_r(i) (b(i-1) - b(i)) \quad [41]$$

for complete relaxation of the youngest layer.

#### G. Recalculation of Elastic Stress in the Scale and SiC Fiber after Radial Displacement

The stress in each  $\text{SiO}_2$  layer can then be recalculated from the new  $\varepsilon_\theta^{\text{SiO}_2}$  by solving the three strain compatibility equations for the three principal stresses:

$$\varepsilon_z^{\text{SiO}_2}(j) = \frac{1}{E_{\text{SiO}_2}} \left[ \sigma_z^{\text{SiO}_2}(j) - \nu_{\text{SiO}_2} \left( \sigma_\theta^{\text{SiO}_2}(j) + \sigma_r^{\text{SiO}_2}(j) \right) \right] \quad [42]$$

$$\varepsilon_\theta^{\text{SiO}_2}(j) = \frac{1}{E_{\text{SiO}_2}} \left[ \sigma_\theta^{\text{SiO}_2}(j) - \nu_{\text{SiO}_2} \left( \sigma_z^{\text{SiO}_2}(j) + \sigma_r^{\text{SiO}_2}(j) \right) \right] \quad [43]$$

$$\varepsilon_r^{\text{SiO}_2}(j) = \frac{1}{E_{\text{SiO}_2}} \left[ \sigma_r^{\text{SiO}_2}(j) - \nu_{\text{SiO}_2} \left( \sigma_\theta^{\text{SiO}_2}(j) + \sigma_z^{\text{SiO}_2}(j) \right) \right] \quad [44]$$

The revised principal stresses in the SiC fiber can then be calculated. The axial stress  $\sigma_z^{\text{SiC}}$  is computed from the total force exerted by the SiO<sub>2</sub> layers which is the sum of the axial stress in each annular SiO<sub>2</sub> element  $\times$  area of that element:

$$\sigma_z^{\text{SiC}}(i) = - \sum_{j=1}^{i-1} \frac{\sigma_z^{\text{SiO}_2}(j)[2c(i)(w(j) - w(j-1) + w(j)^2 - w(j+1)^2)]}{b(i)^2} \quad [45]$$

The revised radial and hoop stress in the SiC fiber can be computed in a similar manner, by computing the net pressure ( $p_n$ ) from the sum of the pressures in each annular layer:

$$\sigma_r^{\text{SiC}}(i) = \sigma_\theta^{\text{SiC}}(i) = -p_n = - \sum_{j=1}^{i-1} \sigma_\theta^{\text{SiO}_2}(j) \frac{w(j) - w(j-1)}{b(i)} \quad [46]$$

These revised stresses are changed incrementally for strain compatibility and stress relaxation as the program loops back to equations [1 - 41] as the next layer  $i$  is considered. For SiC oxidation when  $w(i) \ll b(i)$ , the stress in SiO<sub>2</sub> is much larger than that in SiC and can be neglected for approximate calculations.

### III. Results and Discussion

#### A. General

Growth stress calculations were done using equations [1-46] in a Mathematica™ program. Calculations were done with 50 to 2000 layers ( $i = 50$  to 2000). Variations in calculations were usually insignificant for  $i > 100$ . A value of  $i = 500$  was chosen as an optimal trade-off between precision and calculation speed.

Calculations were done for oxidation of Hi-Nicalon™-S SiC fiber for amorphous scales of 10, 100, 1000, and 3000 nm thickness ( $w$ ) at 700, 800, 900, 1000, 1100, 1200, and 1300°C. The Deal-Grove oxidation kinetics for this fiber have been reported for dry air between 700 and 1300°C with  $A_o = 6.5 \times 10^{-4}$  m,  $B_o = 1.2 \times 10^{-8}$  m<sup>2</sup>/s,  $Q_A = 111$  kJ/mol, and  $Q_B = 249$  kJ/mol.<sup>5-6</sup> The fiber radius ( $b_o$ ) is 6.1  $\mu$ m. The molar volumes for SiC ( $\Omega_{\text{SiC}}$ ) and amorphous SiO<sub>2</sub> ( $\Omega_{\text{SiO}_2}$ ) are 27.34 cm<sup>3</sup> and 12.46 cm<sup>3</sup>, respectively. The Young's modulus ( $E$ ) and Poisson's ratio ( $\nu$ ) values used for SiC and SiO<sub>2</sub> were  $E_{\text{SiC}} = 400$  GPa,  $\nu_{\text{SiC}} = 0.157$ ,  $E_{\text{SiO}_2} = 70$  GPa, and  $\nu_{\text{SiO}_2} = 0.17$ . The shear modulus value used for silica ( $G$ ) was 34 GPa. The continuous variation in growth stress with change in fiber radius was examined by calculations using  $b_o = 3$   $\mu$ m and  $b_o = \rightarrow \infty$  (1 km).

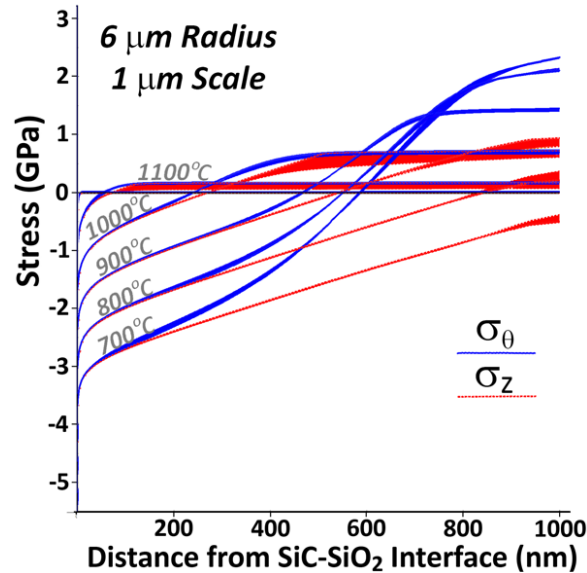


Fig. 4. Hoop stress ( $\sigma_\theta$ ) and axial stress ( $\sigma_z$ ) for a 1  $\mu$ m thick scale on a Hi-Nicalon™-S (6  $\mu$ m radius) fiber calculated using the “High  $\tau$  Method” [29-35] and “Low  $\tau$  Method” [36]. Differences in calculated values between the two methods are small. Compressive values are negative.

General features for hoop stress ( $\sigma_\theta$ ) and axial stress ( $\sigma_z$ ) are evident in figure 4 for a 1  $\mu$ m thick scale on a Hi-Nicalon™-S (6  $\mu$ m radius) fiber. Qualitatively, these results are most similar to those of Delph for elastic-viscoplastic scales during silicon oxidation.<sup>20</sup> Compressive elastic stress of  $\sim -25$  GPa for  $\sigma_\theta$  and  $\sigma_z$  is rapidly relaxed by the Eyring model [23] for SiO<sub>2</sub> glass viscosity ( $\eta$ ) to  $\sim -3$  GPa at 700°C and  $-1$  GPa at 1000°C just 10 nm away from the SiC-SiO<sub>2</sub> interface. This quickly reduces the problem to one similar to unidirectional radial expansion with a residual “intrinsic strain” parallel to the SiC-SiO<sub>2</sub> interface. However, this “intrinsic strain” is T and t dependent,

and the calculations done using unidirectional radial expansion show only tensile  $\sigma_\theta$ , with no transition from compressive to tensile stress.<sup>20, 25</sup>

At the scale surface,  $\sigma_\theta$  is  $\sim 2$  GPa (tension) at 700° and 800°C, and  $\sigma_z$  is  $\sim 1$  GPa (tension) at 700°C.  $\sigma_z$  is driven towards tensile values by the Poisson effect from radial expansion that creates

tensile  $\sigma_\theta$ . Viscous stress relaxation reduces all growth stresses to  $< 100$  MPa at 1100°C and  $< 10$  MPa at 1300°C everywhere in the SiO<sub>2</sub> scale except the region immediately adjacent to the SiC-SiO<sub>2</sub> interface.

Radial stress ( $\sigma_r$ ) calculated by the “High  $\tau$  Method” [29-35] for a 1  $\mu\text{m}$  thick scale on a Hi-Nicalon<sup>TM</sup>-S (6  $\mu\text{m}$  radius) fiber is shown in figure 5 and shear stress ( $\tau$ ) is shown in figure 6. Compressive  $\sigma_r$  up to  $\sim 100$  MPa is present in the center of the scale at 700° - 900°C. This is a consequence of tensile  $\sigma_\theta$  at the scale surface. At 700° - 800°C  $\sigma_r$  goes tensile at the SiC-SiO<sub>2</sub> interface, which is a consequence of the high compressive  $\sigma_\theta$  near that interface.

$\tau$  of  $\sim 12$  GPa is rapidly relaxed to  $\sim 2$  GPa at 700°C and 500 MPa at 1100°C just 10 nm away from the SiC-SiO<sub>2</sub> interface (Fig. 6). It continues to decrease as compressive  $\sigma_z$  and  $\sigma_\theta$  decreases away from the SiC-SiO<sub>2</sub> interface until  $\sigma_\theta$  becomes tensile, at which point  $\tau$  increases towards the SiO<sub>2</sub> surface, reaching surface values close to 1.5 GPa at 700°C and 300 MPa at 1000°C. The shear stress minimum is  $\sim 600$  nm from the SiC-SiO<sub>2</sub> interface at 700°C, 200 nm at 1000°C, and  $\sim 50$  nm at 1100°C. Note that a 1  $\mu\text{m}$  scale takes  $\sim 10^9$  s to form at 700°C and  $\sim 10^6$  s to form at 1000°C, so the latter is of more practical interest.

The practical use of the growth stress calculation method is likely to be limited by knowledge of accurate values for amorphous silica viscosity. Unlike silicon oxidation, silica scales formed during SiC oxidation incorporate carbon.<sup>49-52</sup> Network carbon in amorphous SiO<sub>2</sub> stiffens the network structure, making it more viscous and less permeable to O<sub>2</sub>.<sup>45, 53-54</sup> However, SiO<sub>2</sub> viscosity may be reduced by incorporation of the Cl (620 ppm), S (52 ppm), Ca (45 ppm), Na (35 ppm), and Fe (27 ppm) impurities in Hi-Nicalon<sup>TM</sup>-S fiber.<sup>6</sup>

### B. Comparison of Methods for Calculation of Relaxed Principal Stresses

Two methods for calculation of the relaxed principal stresses from the relaxed shear stress were developed (equations [29-36]). These methods are compared for a 1000 nm thick amorphous SiO<sub>2</sub> scale on a 6  $\mu\text{m}$  radius Hi-Nicalon<sup>TM</sup>-S fiber at 700° - 1300°C in figure 4. The differences between the methods are illustrated by the thickness of the colored lines. For  $\sigma_\theta$  there is little difference between the two methods.

The “Low  $\tau$  Method” [36] finds  $\sigma_\theta$  values slightly lower in absolute value than the “High  $\tau$  Method” [29-35]. In the compressive stress regions of the scale (negative values, close to the SiC-SiO<sub>2</sub> interface) the calculated values for axial stress ( $\sigma_z$ ) are nearly identical. Close to the surface it is higher (more tensile) at 700° and 800°C and lower (less tensile) for higher temperatures. At 1100°C and higher, stresses are rapidly relaxed by viscous flow. There is a 2 $\times$  relative difference in calculated values of  $\sigma_z$  between the two methods, but the absolute difference is small because stresses are low ( $\sim 100$  MPa) and highly relaxed by viscous flow. Since high scale stresses

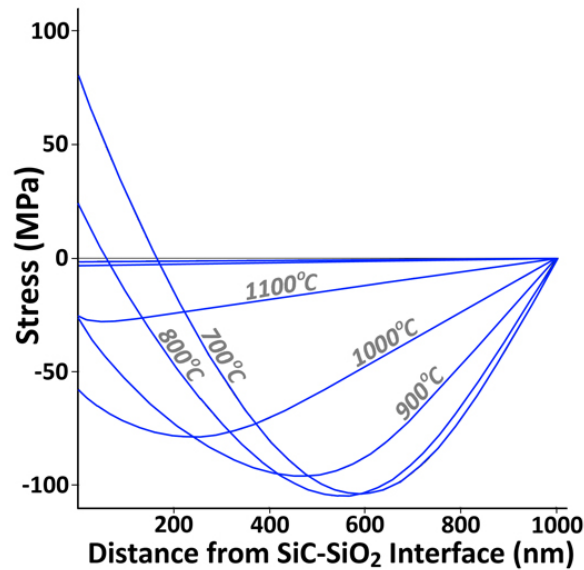


Fig. 5. Radial stress ( $\sigma_r$ ) for a 1  $\mu\text{m}$  thick scale on a Hi-Nicalon<sup>TM</sup>-S (6  $\mu\text{m}$  radius) fiber calculated using the “High  $\tau$  Method” [29-35].

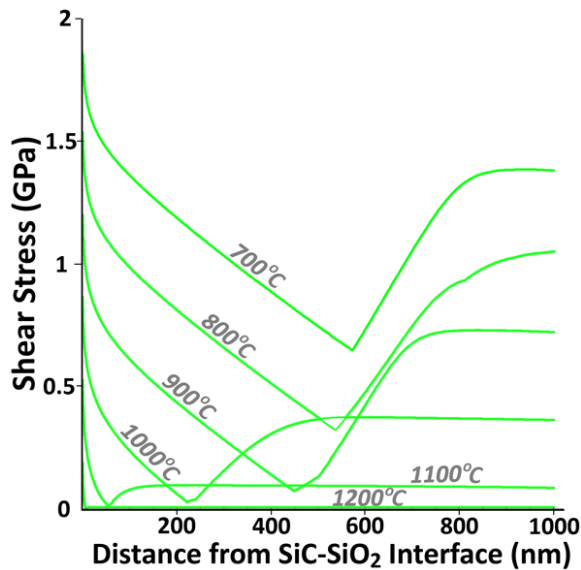


Fig. 6. Shear stress ( $\tau$ ) for a 1  $\mu\text{m}$  thick scale on a Hi-Nicalon<sup>TM</sup>-S (6  $\mu\text{m}$  radius) fiber calculated using the “High  $\tau$  Method” [29-35].

in absolute value than the “High  $\tau$  Method” [29-35]. In the compressive stress regions of the scale (negative values, close to the SiC-SiO<sub>2</sub> interface) the calculated values for axial stress ( $\sigma_z$ ) are nearly identical. Close to the surface it is higher (more tensile) at 700° and 800°C and lower (less tensile) for higher temperatures. At 1100°C and higher, stresses are rapidly relaxed by viscous flow. There is a 2 $\times$  relative difference in calculated values of  $\sigma_z$  between the two methods, but the absolute difference is small because stresses are low ( $\sim 100$  MPa) and highly relaxed by viscous flow. Since high scale stresses

are generally of more interest for structural SiC fibers, further calculations are presented from the “High  $\tau$  Method”.

### C. Variation with Scale Thickness and Fiber Radius

Calculations for 3  $\mu\text{m}$  radius ( $b_0$ ), 6  $\mu\text{m}$  radius, and a flat plate for 10 nm, 100 nm, and 1  $\mu\text{m}$  thick ( $w$ ) scales at 700 - 1300°C are shown in figure 7. The continuous change of  $\sigma_\theta$  and  $\sigma_z$  with change in  $b_0$

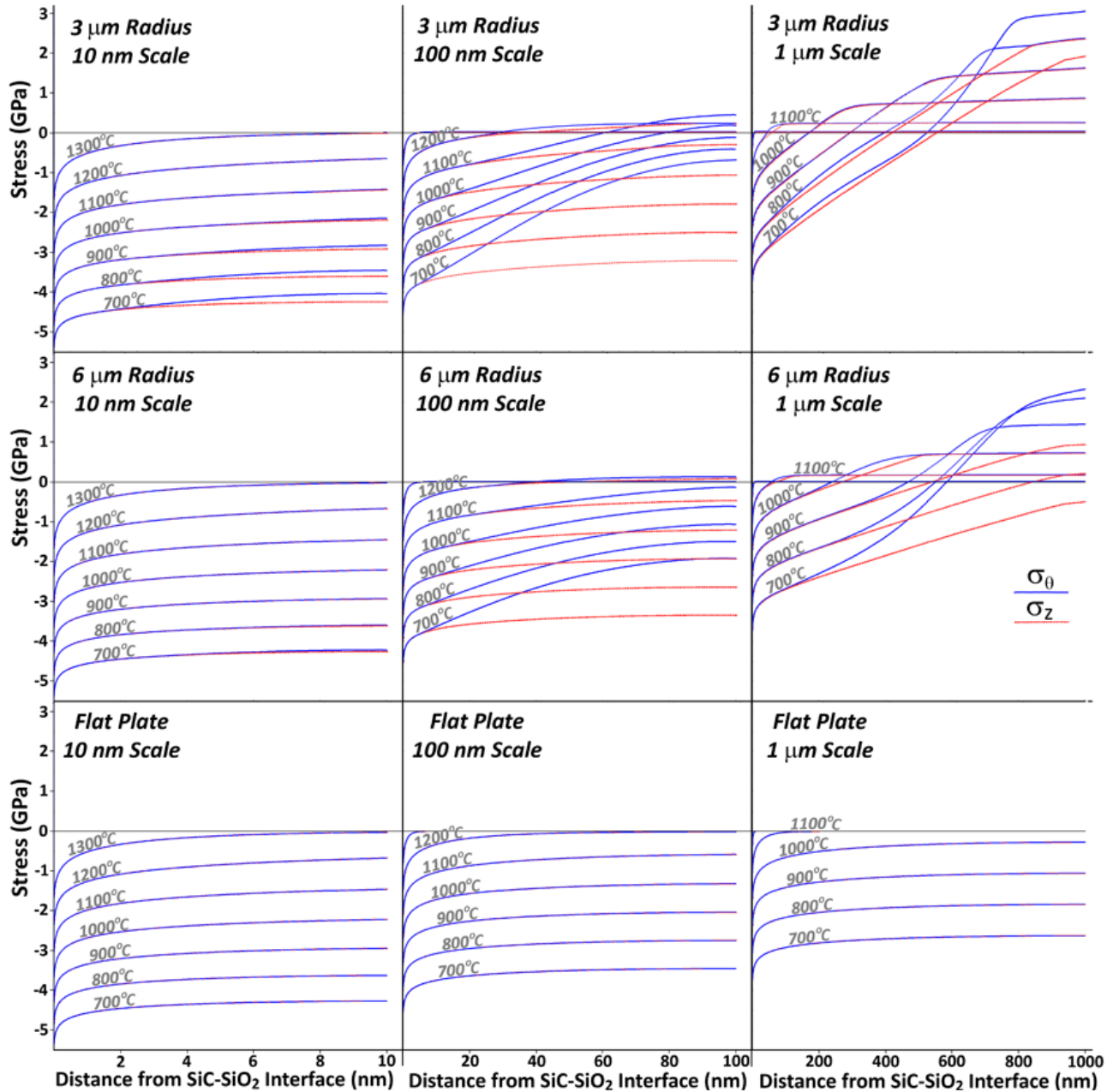


**Fig. 7.** Hoop ( $\sigma_\theta$ ) and axial oxidation growth stress ( $\sigma_z$ ) levels as a function of position in the SiO<sub>2</sub> scale for SiC flat plates and fibers with 6 and 3  $\mu\text{m}$  radius ( $b_0$ ). Results for  $w = 10$  nm, 100 nm, and 1  $\mu\text{m}$  thick scales are shown for temperatures of 700°, 800°, 900°, 1000°, 1100°, 1200°, and 1300°C. The continuous change in both  $\sigma_\theta$  and  $\sigma_z$  with the variables of scale position, temperature ( $T$ ), scale thickness ( $w$ ), and fiber radius ( $b_0$ ) is evident.

and  $w$  at 700°C to 1300°C throughout the scale is evident. For flat plates of  $\sigma_\theta = \sigma_z$ , and stress is always compressive. Growth stress for  $w = 10$  nm is very similar to that of a flat plate for  $b_0 = 3$  and 6  $\mu\text{m}$ .

For a 3  $\mu\text{m}$  radius fiber, tensile  $\sigma_\theta$  develops at the scale surface at temperatures over 950°C for  $w = 100$  nm and reaches values of 400 MPa at 1100°C. Tensile  $\sigma_z$  does not develop until  $T > 1150^\circ\text{C}$  and reaches 100 MPa at 1200°C. For a 6  $\mu\text{m}$  radius fiber, tensile stress does not develop at the scale surface until temperatures close to 1200°C are reached; maximum tensile  $\sigma_\theta$  and  $\sigma_z$  of 100 MPa forms at 1200°C. For both  $b_0 = 3$  and 6  $\mu\text{m}$  with  $w = 100$  nm,  $\sigma_z$  is generally much more compressive than  $\sigma_\theta$ , except at the highest temperatures stresses are almost completely relaxed.

The results for  $w = 1 \mu\text{m}$  scales with  $b_0 = 6 \mu\text{m}$  were discussed in the previous section. Maximum tensile  $\sigma_\theta$  reaches 2.3 GPa and 3 GPa for  $b_0 = 6$  and 3  $\mu\text{m}$ , respectively, at 700°C. Maximum tensile  $\sigma_z$  reaches 1 GPa (900°C) and 2.2 GPa (800°C) for  $b_0 = 6$  and 3  $\mu\text{m}$ , respectively. Much larger fractions of the scale are under tensile stress for a 1  $\mu\text{m}$  thick scale in comparison to a 100 nm thick scale.

#### D. Surface Stress

For structural SiC fibers the residual stress at the scale surface is of great interest. Tensile stress promotes formation of cracks that can degrade fiber strength.<sup>5-6</sup> Compressive stress may have the opposite effect. The stress values at maximum distance from the SiC-SiO<sub>2</sub> interface in figure 7 are the surface stresses (right hand side of each plot). Calculations for the hoop stress ( $\sigma_\theta$ ) and axial stress ( $\sigma_z$ ) at the scale surface are mapped as a function of temperature (T) and scale thickness (w) in figures 8-10

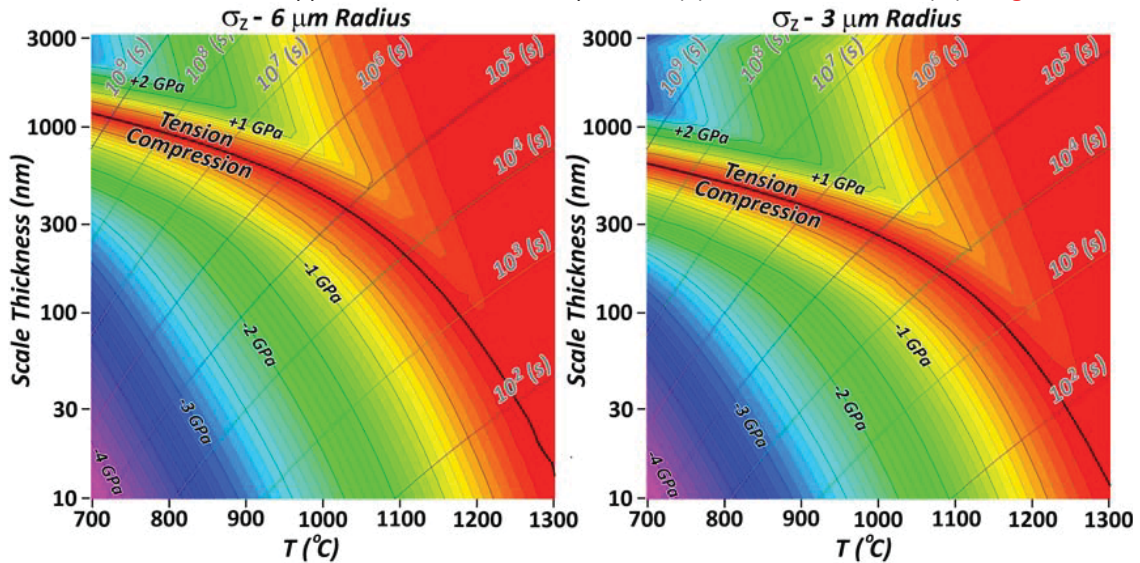


Fig. 8. Axial stress ( $\sigma_z$ ) at the SiO<sub>2</sub> scale surface as a function of scale thickness and oxidation temperature for 6 and 3  $\mu\text{m}$  radius SiC fibers. Oxidation time isochrones are also shown.

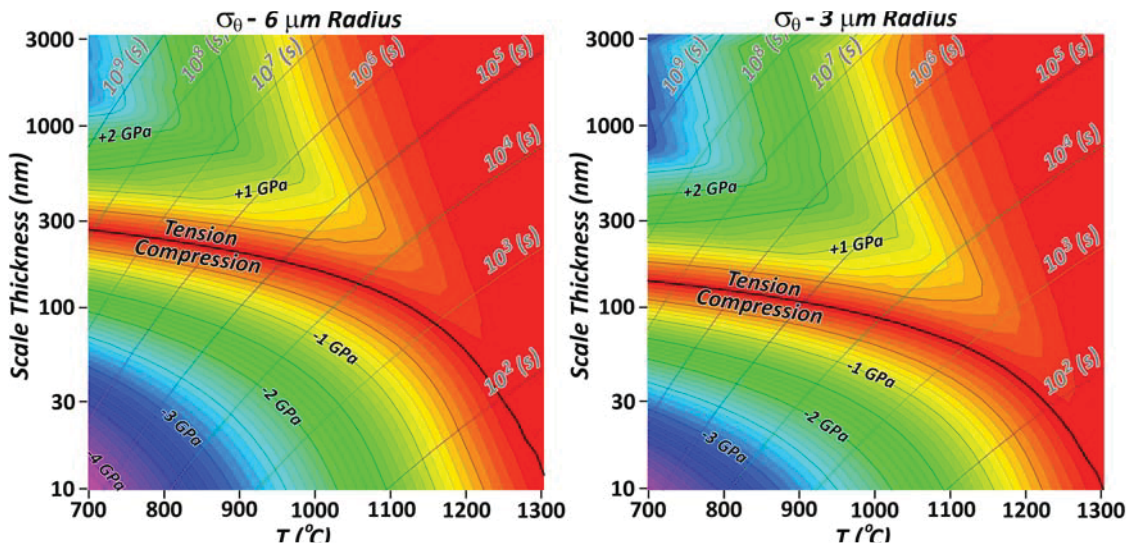


Fig. 9. Hoop stress ( $\sigma_\theta$ ) at the SiO<sub>2</sub> scale surface as a function of scale thickness and oxidation temperature for 6 and 3  $\mu\text{m}$  radius SiC fibers. Oxidation time isochrones are also shown.

for flat plates, 6  $\mu\text{m}$  radius fibers, and 3  $\mu\text{m}$  radius fibers. These plots clearly distinguish tensile and compressive regions, and also show logarithmic time isochrones in seconds.

The tensile stress maximum forms at smaller scale thicknesses as temperature increases. This maximum is the greatest practical concern for structural SiC fibers. The plots illustrate T-t windows that should be avoided. For example, a tensile  $\sigma_z$  of  $\sim 500$  MPa forms for a scale of  $\sim 600$  nm thickness at  $1050^\circ\text{C}$  in  $10^5$  seconds ( $\sim 1$  day) during oxidation of a 6  $\mu\text{m}$  radius fiber in dry air (Fig. 8). For a 3  $\mu\text{m}$  radius fiber this maximum is  $\sim 750$  MPa. Longer oxidation times would decrease, rather than increase, this stress. Much higher tensile stresses are possible at lower temperatures, but require much longer to form, and will form for thicker rather than thinner scales. These high tensile stresses may impact fiber strength at temperature. They are larger than the compressive thermal stresses that will develop in the  $\text{SiO}_2$  scale during cool down ( $\sim 300$  MPa), and so may impact room temperature strength as well.

The maximum tensile  $\sigma_\theta$  that forms at  $1050^\circ\text{C}$  is  $\sim 600$  and  $900$  MPa for 6 and 3  $\mu\text{m}$  radius fibers, respectively (Fig. 9). This stress maximum occurs at a significantly lower scale thickness and shorter time than the  $\sigma_z$  maximum (Fig. 8). Tensile  $\sigma_\theta$  stresses have been suggested to cause axial cracking of scale during oxidation, rendering the scale non-passivating.<sup>5,6</sup> Calculations for a flat plate, where all stresses are compressive, are shown in figure 10 for comparison.

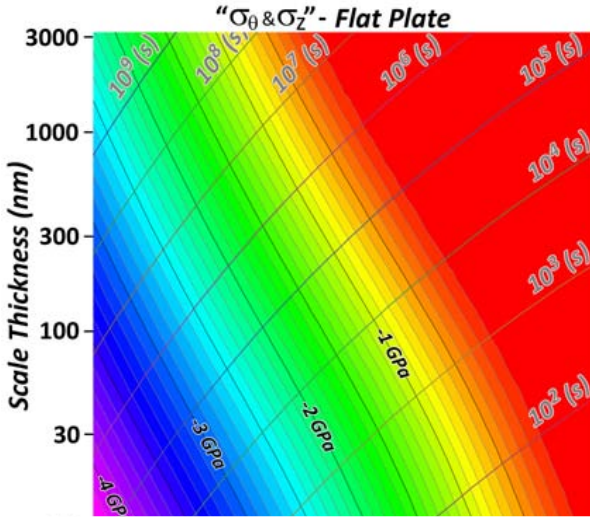


Fig. 10. Stress ( $\sigma_\theta = \sigma_z$ ) at the  $\text{SiO}_2$  scale surface as a function of scale thickness and oxidation temperature. Oxidation time isochrones are also shown.

shown in figure 10 for comparison.

### E. Steady-State Tensile Stress

A near “steady-state” develops for tensile stress at  $T \geq 1200^\circ\text{C}$  for  $w = 100$  nm for both  $b_0 = 3$  and  $6 \mu\text{m}$  (Fig. 7). At lower temperatures, greater scale thickness is required to reach steady-state. A  $w > \sim 1 \mu\text{m}$  is required for  $T \geq 1000^\circ\text{C}$ . The tensile  $\sigma_\theta$  and  $\sigma_z$  values are nearly equal, with little change for significant distances beneath the scale surface (Fig. 7), but the scale thickness (time) required to reach steady-state is longer for  $\sigma_z$  because it is driven to tensile values by the Poisson effect from  $\sigma_\theta$ . For shear stress  $\tau < \tau_c$  of  $100$  MPa [23] where a stress-free viscosity ( $\eta_0$ ) [24] is applicable, a simple expression for the steady-state hoop stress [ $\sigma_\theta(ss)$ ] can be derived. The rate at which scale thickness ( $\delta$ ) is increased from the

oxidation volume increase is:

$$\frac{d\delta}{dt} = \frac{B}{w} \left( \frac{1}{\Omega} - 1 \right) \quad [47]$$

If  $\sigma_r$  is negligible, the shear stress is half the hoop stress, and the rate at which hoop strain ( $\epsilon_\theta$ ) develops in the outer scale is:

$$\frac{d\epsilon_\theta}{dt} = \frac{\tau}{\eta_0} = \frac{\sigma_\theta(ss)}{2\eta_0} = \frac{d\delta}{dt} \quad [48]$$

[47] and [48] can be solved for the steady-state hoop stress  $\sigma_\theta(ss)$ :

$$\sigma_\theta(ss) = \frac{2B \left( \frac{1}{\Omega} - 1 \right) \eta_0}{wb} \quad [49]$$

For  $\tau > 100$  MPa the stress dependence of viscosity is significant, and [23] must be substituted for  $\eta_o$ , giving:

$$\sigma_{\theta}(ss) = -2\tau_c Csch \left[ \frac{bw\tau_c\Omega}{B\eta_o(\Omega - 1)} \right]^{-1} \quad [50]$$

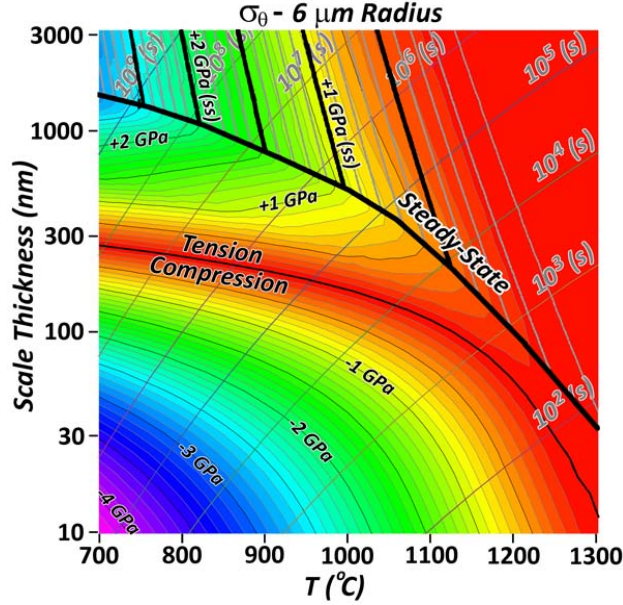


Fig. 11. The plot for surface stress in Fig. 9 for  $b_o = 6 \mu\text{m}$ , with predictions for the steady-state region from [50] superimposed.

Predictions for steady-state  $\sigma_{\theta}$  tensile stress from [50] for a  $6 \mu\text{m}$  radius fiber are shown in figure 11. High temperature ( $> 1150^\circ\text{C}$ ) steady-state stress value predictions are high, but at lower temperatures the prediction is close to calculated values. A steady state develops in  $\sim 2$  minutes at  $1300^\circ\text{C}$ , 3 hours at  $1100^\circ\text{C}$ , and in  $\sim 100$  days at  $900^\circ\text{C}$ . The predictions for  $\sigma_z$  are the same as those for  $\sigma_{\theta}$ , except the times to reach steady state are longer (Fig. 8). For smaller radius fibers the time to reach steady-state is also shorter.

By expanding [49] with the Arrhenius expressions for  $B$  and  $\eta_o$ , the steady-state tensile stress decrease with increasing temperature is evident when  $Q > Q_b$ ; the scale viscosity decreases faster with an increase in temperature than the oxidation rate:

$$\sigma_{\theta}(ss) = \frac{2B_o C_o e^{\frac{Q-Q_b}{RT}} \left( \frac{1}{\Omega} - 1 \right)}{wb} \quad [51]$$

This suggests that if materials exist for which  $Q < Q_b$ , a counterintuitive increase in tensile growth stress with increase in oxidation temperature is expected – the oxidation rate, and growth stress

generation associated with it, will increase faster than the rate at which viscosity decreases.

### F. Crystalline Scale

$\text{SiO}_2$  scale crystallization kinetics have been measured for Hi-Nicalon<sup>TM</sup>-S SiC fiber; crystallization begins after  $\sim 100$  hours at  $1000^\circ\text{C}$  or 1 hour at  $1300^\circ\text{C}$ , when scales are roughly  $500 \text{ nm}$  and  $100 \text{ nm}$  thick, respectively.<sup>5-6</sup> Unfortunately, SiC oxidation kinetics for crystalline scales (cristobalite and tridymite) are not well characterized, and there is even less data on creep rates and/or viscosities. However, it is clear that the oxidation kinetics for crystalline scales are slower.<sup>5-6</sup> Some kinetic data suggests that crystalline scale thicknesses are  $\sim 1/3$  those for amorphous scales.<sup>55-56</sup> Temperature dependence was not reported, so to a first approximation it is assumed that  $B_o$  is an order of magnitude smaller ( $B_o = 1.2 \times 10^{-9} \text{ m}^2/\text{s}$ ) and other Deal-Grove parameters are unchanged. Limited data for creep rates for cristobalite refractories suggests that at  $1550^\circ - 1650^\circ\text{C}$  creep is negligible at very low stress ( $0.2$  to  $0.6 \text{ MPa}$ ), but further quantification was not possible.<sup>36-38</sup>

To explore the possible effects of crystallization on growth stress, we assume that cristobalite viscosity is four orders of magnitude higher than that of amorphous silica at all temperatures:  $C_o = 3.8 \times 10^{-9} \text{ Pa}\cdot\text{s}$  [24]. Calculations are done for a  $1 \mu\text{m}$  thick scale at  $1100^\circ\text{C}$ , and for cases where crystallization occurs when the scale is  $100 \text{ nm}$  thick,  $500 \text{ nm}$  thick, and  $900 \text{ nm}$  thick (Fig. 12). These thicknesses set the value for  $x_i$  in [1]. Crystallization rates are very rapid compared to scale growth rates.<sup>5-6</sup> We assume that during crystallization all stresses in the amorphous  $\text{SiO}_2$  are eliminated and are not transferred into the crystalline product. Calculations for an  $\text{SiO}_2$  glass (Fig. 7) are included for comparison.

At  $1100^\circ\text{C}$ ,  $\sigma_{\theta}$  and  $\sigma_z$  are tensile,  $< 200 \text{ MPa}$ , and in steady-state throughout most of the scale (Fig. 12). For early scale crystallization ( $x_i = 100 \text{ nm}$ ),  $\sigma_{\theta}$  is  $1.6 \text{ GPa}$  (tension) at the scale surface, and  $\sigma_z$  is  $450 \text{ MPa}$  (tension). For  $x_i = 500 \text{ nm}$ , these values are  $700 \text{ MPa}$  and  $150 \text{ MPa}$ , respectively, but a higher tensile  $\sigma_{\theta}$  of  $1.5 \text{ GPa}$  is present at  $x = 500 \text{ nm}$ , with a sharp transition to high compressive stress at

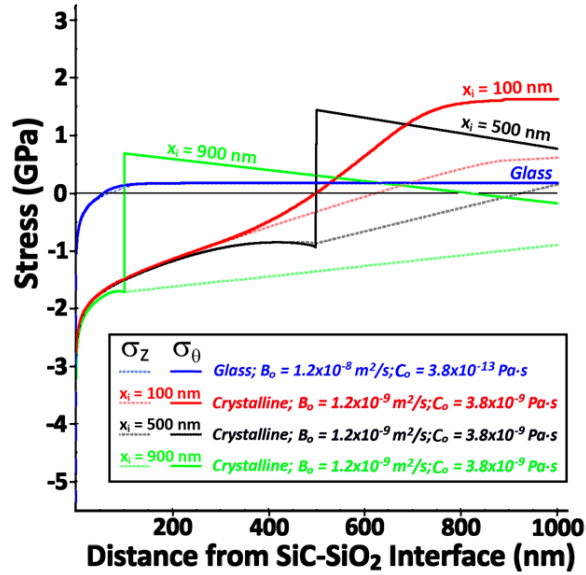


**Fig. 12.** Hoop ( $\sigma_\theta$ ) and axial growth stress ( $\sigma_z$ ) levels after oxidation at 1100°C as a function of position in a crystalline SiO<sub>2</sub> scale for SiC fibers with 6  $\mu\text{m}$  radius ( $b_0$ ). Stress after scale crystallization at  $x_i = 100, 500,$  and  $900$  nm is calculated, as well as glass for comparison.

compressive growth stress and externally applied stress, and the enhancement by externally applied tensile stress was briefly mentioned.<sup>8, 12, 20, 24-25, 29-31</sup> Some data for oxidation enhancement by tensile stress also exists for SiC.<sup>32</sup> Recent work on SiC fiber oxidation finds the oxidation rates tend to be higher than those observed for bulk SiC.<sup>5-6</sup> There was speculation that this could be a SiC substrate geometry effect, related to the development of tensile stress in the fiber scale.

The usual method for handling stress effects on oxidation kinetics is to assume a pressure ( $p$ ) effect on the parabolic rate constant  $B$ :

$$B(p) = B e^{pV_d/kT} \quad [52]$$

where  $V_d$  is an activation volume, calculated to be  $7.5 \times 10^{-29} \text{ m}^3$  for silicon oxidation,<sup>12, 20, 25</sup> and pressure is:

$$p = \frac{1}{3}(\sigma_\theta + \sigma_z + \sigma_r) \quad [53]$$

The pressure clearly varies from high negative values (hydrostatic compression) at the SiC-SiO<sub>2</sub> interface to lower values at the surface; these can reverse sign be in hydrostatic tension for thick scales at low temperatures (Fig. 7).

A first-order correction for the relative effects of growth stress in flat-pale and cylindrical geometries is attempted by calculating the average self-pressure ( $p_{av}$ ) in the SiO<sub>2</sub> scale throughout its thickness, as a function of total scale thickness ( $w$ ), temperature, and fiber radius. This is done by summing the pressure – scale volume product for each scale increment and normalizing by the scale volume:

$$p(av) = \frac{1}{c_1^2 - b_1^2} \sum_{j=1}^i p(b_j^2 - b_{j-1}^2) \quad [54]$$

The average pressure ( $p_{av}$ ) was calculated for 6 and 3  $\mu\text{m}$  radius fibers (Fig. 13) as a function of total scale thickness from 10 to 3000 nm and temperature from 700° to 1300°C. Average pressures of

the point in the scale at which crystallization occurred. For  $x_i = 900$  nm the scale has spent a relatively short time growing in the crystalline state. Surface stresses are compressive, but tensile  $\sigma_\theta$  of 700 MPa develops at  $x = 100$  nm.

As expected, much lower scale viscosities cause much higher stresses. Cracks that form during oxidation in cristobalite and tridymite scales, but not in amorphous scales,<sup>5-6</sup> can clearly be a consequence of the much higher tensile surface stresses ( $> 1$  GPa) that may develop in crystalline SiO<sub>2</sub> scales. Porosity present in the centers of crystalline scales might also be inferred to be a consequence of hydrostatic tension that develops at the point in the scale at which crystallization occurred. Crystalline SiO<sub>2</sub> will deform by dislocation plasticity at high  $\tau$ ; mechanisms implicit in the Eyring model for glass no longer apply. There is evidence for intense dislocation plasticity in crystalline SiO<sub>2</sub> scale near the SiC-SiO<sub>2</sub> interface.<sup>5-6</sup> The 20 nm of SiO<sub>2</sub> adjacent to SiC will have  $\tau > 1$  GPa, which is more than enough for domination of creep by dislocation-based mechanisms.<sup>57</sup>

### G. Effects of Stress on Oxidation Rate

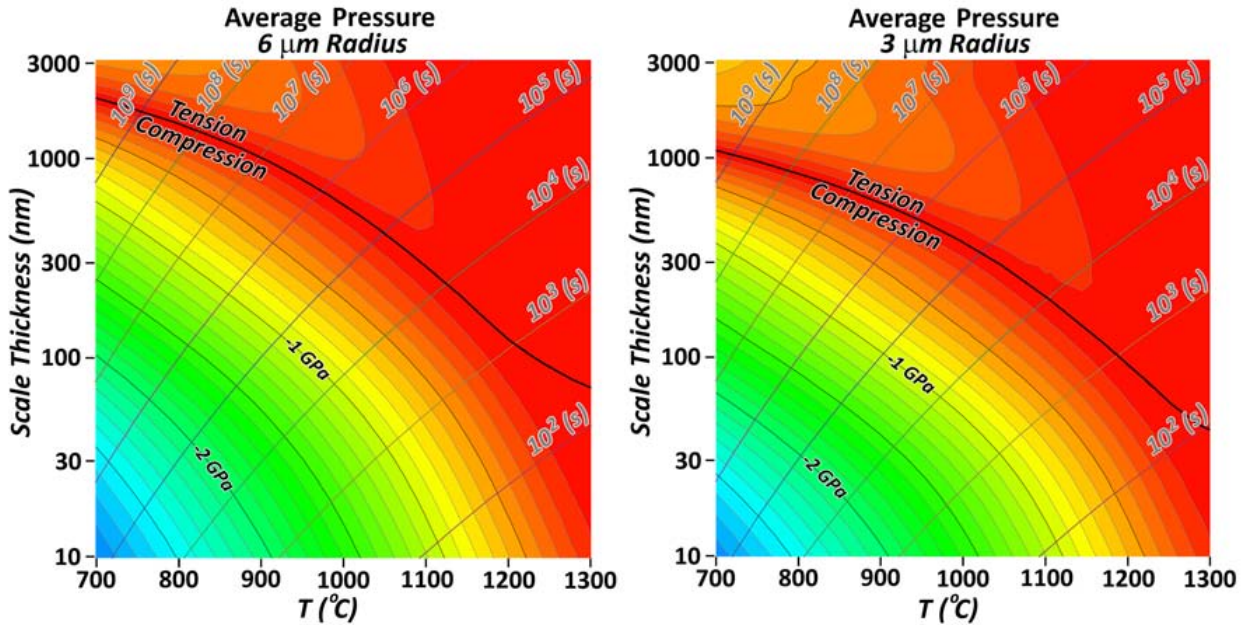


Fig. 13. Average SiO<sub>2</sub> scale self-pressure ( $p_{av}$ ) for 6 and 3  $\mu\text{m}$  radius fibers as a function of scale thickness ( $w$ ) and temperature

>2.5 GPa (compression) and >300 MPa (tension) were calculated for thin and thick scales, respectively, at low temperatures. Scales formed at high temperature do not support significant self-pressures.

When comparing oxidation rates for bulk and fiber SiC, the difference in self-pressure between the two geometries is relevant. Both geometries have scale pressure. Calculations for the flat plate geometry are shown in figure 14. The difference in average pressure ( $\Delta p_{av}$ ) between a flat plate and a 6  $\mu\text{m}$  radius fiber is shown in figure 15. Fibers with thick scales formed at low temperatures have the

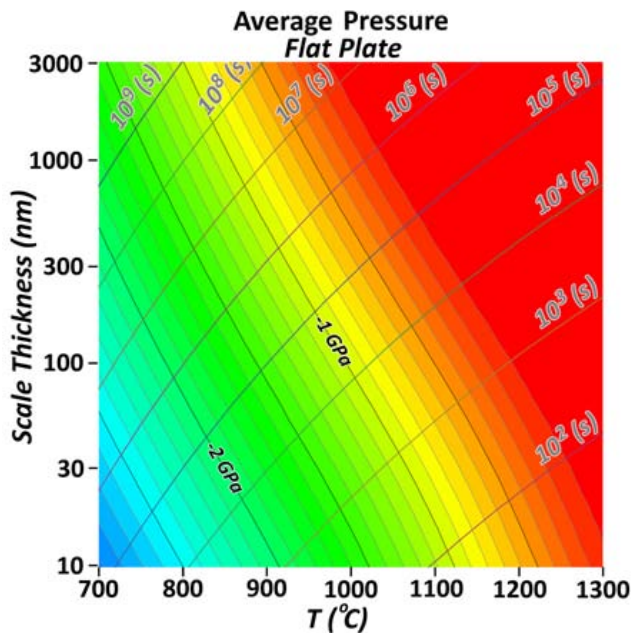


Fig. 14. Average SiO<sub>2</sub> scale self-pressure ( $p_{av}$ ) for a flat plate as a function of scale thickness ( $w$ ) and temperature

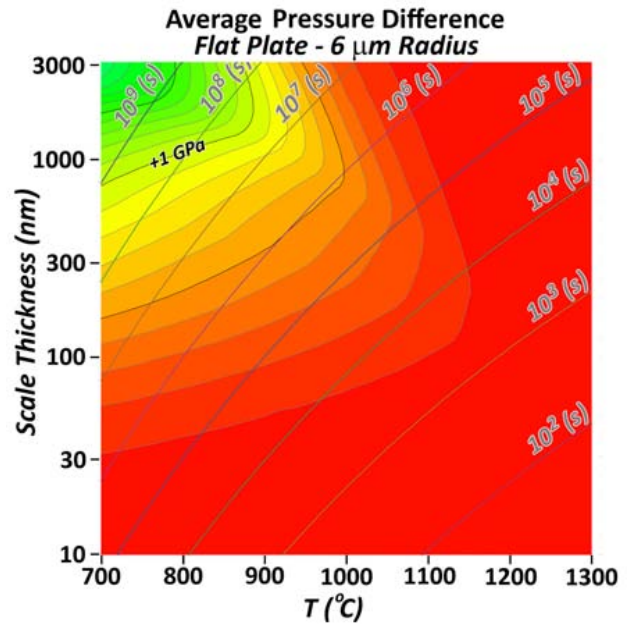


Fig. 15. The difference in average SiO<sub>2</sub> scale self-pressure ( $\Delta p_{av}$ ) between a flat-plate and a 6  $\mu\text{m}$  radius fiber as a function of scale thickness ( $w$ ) and temperature.

greatest  $\Delta p_{av}$ , and should therefore show the greatest enhancement relative to flat-plate oxidation kinetics.

For previously reported oxidation data for Hi-Nicalon<sup>TM</sup>-S SiC fiber,<sup>5-6</sup> the highest  $\Delta p_{av}$  is ~500 MPa for ~1  $\mu\text{m}$  thick SiO<sub>2</sub> scales formed at 1000°C (Fig. 15). By [52], the lower growth stresses (relative to flat plates) in fibers oxidized under these conditions would enhance **B** by ~8.5× in comparison to flat plates, increasing scale thickness by ~3×. This is at best only a partial explanation for the relatively high SiC oxidation rates for Hi-Nicalon<sup>TM</sup>-S fiber. Most data, particularly that at 700° - 900°C and 1200° - 1300°C, has much lower  $\Delta p_{av}$  and the effects of growth stress would be insignificant.

It is interesting to note that the data of Gauthier et al. for stress dependence of the parabolic rate constant for Hi-Nicalon<sup>TM</sup> SiC fiber oxidation at 800°C is consistent with an 8× enhancement at ~500 MPa.<sup>32</sup> However, at higher stresses it is no longer consistent with [52].<sup>32</sup> At 1.276 GPa there is a measured enhancement of 19×, but [52] predicts enhancement by ~600×. We suggest that this is due to stress relaxation in the SiO<sub>2</sub> scale by [23], since shear stress is well above  $\tau_c$ .

#### IV. Summary and Conclusions

A method to calculate the axial, hoop, and radial growth stresses in SiO<sub>2</sub> scales for the 2.2× volume expansion during SiC fiber oxidation was developed. Axial stresses are usually ignored, but for structural fibers they have the largest effect on strength. The method assumes oxidation volume expansion is three-dimensional (dilatational) and that the stresses resulting from constraint of that expansion are relaxed radially with an Eyring stress-dependent SiO<sub>2</sub> viscosity, although other appropriate viscosity models can be substituted. The method can be equally well applied to fibers of silicon or other materials. High compressive hoop and axial stresses of ~25 GPa are very quickly relaxed to much lower values at all temperatures. Stresses relax by radial expansion, which creates tensile hoop stress in the outer scale. Tensile hoop stress eventually drives axial stress to a tensile state by the Poisson effect. Tensile hoop and axial stress can reach values greater than 2 GPa for long times at 700° and 800°C. A continuum in stress response from flat plate geometry to small fiber radius geometry is demonstrated. The accuracy of the growth stress calculation method is limited by knowledge of accurate values for amorphous silica viscosity, which can be affected by incorporation of carbon or other impurities during SiC oxidation.

Tensile hoop and axial stresses reach steady-state values that can be described by analytical expressions. At steady-state, tensile stress relaxation rates are counterbalanced by hoop stress generation tied to the radial expansion of scale and the oxidation rate. At temperatures over 1200°C all growth stresses are rapidly relaxed by viscous flow to very low values. For Hi-Nicalon<sup>TM</sup>-S SiC fibers, a 900°-1100°C oxidation temperature – 300 nm - 1  $\mu\text{m}$  scale thickness window may exist where high tensile stresses at the scale surface are likely to develop. These may have negative effects on fiber mechanical properties. Even higher tensile stresses may develop for thicker scales at lower temperatures, but the times required to reach those thicknesses are very long.

Crystalline SiO<sub>2</sub> scales are assumed to have much higher viscosities than amorphous scales, and should therefore develop much higher tensile hoop and axial stresses than those scales. Unfortunately, lack of data on cristobalite and tridymite viscosity or creep rates, as well as diffusion rates, prohibits accurate quantitative prediction. However, qualitative predictions of high tensile stress in the outer scale and high shear stress near the SiC-SiO<sub>2</sub> interface are consistent with microstructure observations in crystalline silica scales.

Sample geometry may affect oxidation rates through the geometric effect on growth stresses. A Hi-Nicalon<sup>TM</sup>-S SiC fiber and a flat plate of the same composition are calculated to have up to a ~500 MPa difference in average SiO<sub>2</sub> scale pressure from growth stress in thick scales formed at ~1000°C. This could increase scale thickness in the fiber by ~3× over that of the flat plate. However, the effect is smaller at higher and lower temperatures, and is currently only a partial explanation for higher fiber oxidation rates.

#### References

1. V. Presser and K. G. Nickel, Crit. Rev. Solid State Mater. Sci. **33**, 1-99 (2008).
2. I. Vickridge, J. Ganem, Y. Hoshino and I. Trimaille, J. Physics D: Applied Physics **40** (20), 6254 (2007).

3. G. Chollon, M. Czerniak, R. Pallier, X. Bourrat, R. Naslain, J. P. Pillot and R. Cannet, *J. Mater. Sci.* **32**, 893-911 (1997).
4. G. Chollon, R. Pallier, R. Naslain, F. Laanani, M. Monthieux and P. Olry, *J. Mater. Sci.* **32**, 327-347 (1997).
5. R. S. Hay, G. E. Fair, R. Bouffieux, E. Urban, J. Morrow, A. Hart and M. Wilson, *Ceram. Eng. Sci. Proc.* **32**, accepted (2011).
6. R. S. Hay, G. E. Fair, R. Bouffieux, E. Urban, J. Morrow, J. Somerson, A. Hart and M. Wilson, *J. Am. Ceram. Soc.* (2011 in press).
7. C. H. Hsueh and A. G. Evans, *J. Appl. Phys.* **54** (11), 6672-6686 (1983).
8. K. Garikipati and V. S. Rao, *J. Computational Physics* **174** (1), 138-170 (2001).
9. V. S. Rao and T. J. R. Hughes, *Int. J. Numerical Methods in Engineering* **47** (1-3), 341-358 (2000).
10. E. P. EerNisse, *Appl. Phys. Lett.* **35** (1), 8-10 (1979).
11. S. M. Hu, *J. Appl. Phys.* **70** (6), R53-R80 (1991).
12. V. Senez, D. Collard, B. Baccus, M. Brault and J. Lebaillay, *J. Appl. Phys.* **76** (6), 3285-3295 (1994).
13. T. Uchida, M. Fujinaga, N. Kotani, S. Kawazu and H. Miyoshi, *Jap. J. Appl. Phys.* **35** (8), 4265-4273 (1996).
14. T. Uchida and K. Nishi, *Jap. J. Appl. Phys.* **40** (12), 6711-6719 (2001).
15. J. D. Evans, M. Vynnycky and S. P. Ferro, *J. Eng. Math.* **38**, 191-218 (2000).
16. M. Uematsu, H. Kageshima, K. Shiraishi, M. Nagase, S. Horiguchi and Y. Takahashi, *Solid-State Electronics* **48** (6), 1073-1078 (2004).
17. J. P. Peng, D. Chidambarrao and G. R. Srinivasan, *COMPEL* **10** (4), 341-353 (1993).
18. P. Causin, M. Restelli and R. Sacco, *Computer Methods in Applied Mechanics and Engineering* **193** (33-35), 3687-3710 (2004).
19. A. Pomp, S. Zelenka, N. Strecker and W. Fichtner, *IEEE Trans. Elec. Dev.* **47** (10), 1999-2007 (2000).
20. T. J. Delph, *J. Appl. Phys.* **83** (2), 786-792 (1998).
21. D.-B. Kao, J. P. McVittie, W. D. Nix and K. C. Saraswat, *IEEE Trans. Electron. Dev.* **35** (1), 25-37 (1988).
22. C. S. Rafferty, L. Borucki and R. W. Dutton, *Appl. Phys. Lett.* **54** (16), 1516-1518 (1989).
23. N. F. Mott, S. Rigo, F. Rochet and A. M. Stoneham, *Philos. Mag. B* **60** (2), 189-212 (1989).
24. M. Navi and S. T. Dunham, *J. Electrochem. Soc.* **144** (1), 367-371 (1997).
25. P. Sutardja and W. G. Oldham, *Electron Devices, IEEE Transactions on* **36** (11), 2415-2421 (1989).
26. R. H. Doremus, *Thin Solid Films* **122** (3), 191-196 (1984).
27. K. Imai and K. Yamabe, *J. Appl. Phys.* **83** (7), 3849-3855 (1998).
28. R. B. Marcus and T. T. Sheng, *J. Electrochem. Soc.* **129** (6), 1278-1282 (1982).
29. A. Mihalyi, R. J. Jaccodine and T. J. Delph, *Appl. Phys. Lett.* **74** (14), 1981-1983 (1999).
30. J.-Y. Yen and J.-G. Hwu, *Appl. Phys. Lett.* **76** (14), 1834-1835 (2000).
31. J.-Y. Yen and J.-G. Hwu, *J. Appl. Phys.* **89** (5), 3027-3032 (2001).
32. W. Gauthier, F. Pailler, J. Lamon and R. Pailler, *J. Am. Ceram. Soc.* **92** (9), 2067-2073 (2009).
33. E. Oh, J. Walton, D. Lagoudas and J. Slattery, *Acta Mechanica* **181** (3), 231-255 (2006).
34. C. S. Rafferty and R. W. Dutton, *Appl. Phys. Lett.* **54** (18), 1815-1817 (1989).
35. H. Eyring, *J. Chem. Phys.* **4**, 283-291 (1936).
36. A. A. Wereszczak, M. Karakus, K. C. Liu, B. A. Pint, R. E. Moore and T. P. Kirkland, *ORNL/TM-13757*, 1-61 (1999).
37. A. A. Wereszczak, K. Breder, M. K. Ferber, T. P. Kirkland, E. A. Payzant, C. J. Rawn, E. Krug, C. L. Larocco, R. A. Pietras and M. Karakus, *J. Mater. Sci.* **37** (19), 4235-4245 (2002).
38. M. K. Ferber, A. A. Wereszczak and J. G. Hemrick, *Final Technical Report ORNL/TM-2005/134*, 1-67 (2006).

39. L. O. Wilson and R. B. Marcus, *J. Electrochem. Soc.* **134** (2), 481-490 (1987).
40. B. E. Deal and A. S. Grove, *J. Appl. Phys.* **36** (12), 3770-3778 (1965).
41. Y. C. Tsui and T. W. Clyne, *Thin Solid Films* **306**, 34-51 (1997).
42. P. P. Donnadieu, O. Jaoul and M. Kleman, *Philos. Mag. A* **52** (1), 5-17 (1985).
43. R. H. Doremus, *J. Appl. Phys.* **92** (12), 7619-7629 (2002).
44. G. Hetherington, K. H. Jack and J. C. Kennedy, *Phys. Chem. Glasses* **5** (5), 130-136 (1964).
45. T. Rouxel, G.-D. Soraru and J. Vicens, *J. Am. Ceram. Soc.* **84** (5), 1052-1058 (2001).
46. J. H. Li and D. R. Uhlmann, *J. Non. Cryst. Sol.* **3** (1), 127-147 (1970).
47. L. E. Malvern, *Introduction to the Mechanics of a Continuous Medium*, 1st ed. (Prentice-Hall, 1969).
48. A. Polian and et al., *Europhys. Lett.* **57** (3), 375 (2002).
49. T. Narushima, M. Kato, S. Murase, C. Ouchi and Y. Iguchi, *J. Am. Ceram. Soc.* **85** (8), 2049-2055 (2002).
50. M. I. Chaudhry, *J. Mater. Res.* **4** (2), 404-407 (1989).
51. C. E. Ramberg, G. Cruciani, K. E. Spear, R. E. Tressler and C. F. Ramberg, *J. Am. Ceram. Soc.* **79** (11), 2897-2911 (1996).
52. U. J. T. Ogbuji and E. J. Opila, *J. Electrochem. Soc.* **142**, 925-930 (1995).
53. G. M. Renlund, S. Prochazka and R. H. Doremus, *J. Mater. Res.* **6** (12), 2723-2734 (1991).
54. T. Rouxel, G. Massouras and G.-D. Soraru, *J. Sol-Gel Sci. Tech.* **14**, 87-94 (1999).
55. V. Presser, A. Loges, Y. Hemberger and K. G. Nickel, *J. Am. Ceram. Soc.* **92** (3), 724-731 (2009).
56. V. Presser, A. Loges, Y. Hemberger and K. G. Nickel, *J. Am. Ceram. Soc.* **92** (8), 1796-1805 (2009).
57. H. J. Frost and M. F. Ashby, *Deformation Mechanism Maps*. (Pergamon Press, 1982).